An Atlas of Computed Equivalent Widths of Quasar Broad Emission Lines

Kirk Korista
Department of Physics & Astronomy, University of Kentucky, Lexington, KY 40506

Jack Baldwin
Cerro Tololo Interamerican Observatory[1], Casilla 603, La Serena, Chile

Gary Ferland & Dima Verner
Department of Physics & Astronomy, University of Kentucky, Lexington, KY 40506

ABSTRACT

We present graphically the results of several thousand photoionization calculations of broad emission line clouds in quasars, spanning seven orders of magnitude in hydrogen ionizing flux and particle density. The equivalent widths of 42 quasar emission lines are presented as contours in the particle density – ionizing flux plane for a typical incident continuum shape, solar chemical abundances, and cloud column density of $N(H) = 10^{23}$ cm^{-2}. Results are similarly given for a small subset of emission lines for two other column densities (10^{22} cm^{-2} and 10^{24} cm^{-2}), five other incident continuum shapes, and a gas metallicity of 5 $Z_{\odot}$. These graphs should prove useful in the analysis of quasar emission line data and in the detailed modeling of quasar broad emission line regions. The digital results of these emission line grids and many more are available over the Internet.

Subject headings: quasars: emission lines – atlases

[1]Operated by the Association of Universities for Research in Astronomy Inc. (AURA) under cooperative agreement with the National Science Foundation

1. Introduction

Early photoionization calculations could roughly reproduce the average observed quasar broad emission line (BEL) spectrum in a single "cloud"; i.e. one with a single column density ($N(H) \sim 10^{23}$ cm^{-2}), gas density ($\sim 10^{10}$ cm^{-3}), and ionization parameter ($U \equiv n_{ph}/n_e \sim 0.01$) (Davidson 1977, Davidson & Netzer 1979, Kwan & Krolik 1981). However, in the past decade, spectroscopic observations have pointed to the presence of a wide distribution in the emission line cloud properties within each quasar (Gaskell 1982; Wilkes 1984; Espey et al. 1989; Corbin 1989; Clavel et al. 1991; Peterson 1993), prompting the more recent multi-cloud, single pressure law calculations by Rees, Netzer, & Ferland (1989), Krolik et al. (1991), Goad, O'Brien, & Gondhalekar (1993), and O'Brien, Goad, & Gondhalekar (1994, 1995). Most recently, Baldwin et al. (1995) found that simply integrating the emission from a wide distribution in cloud gas properties (gas density, ionizing flux, and column density) results in a spectrum that is consistent with composite quasar spectra and may offer simple solutions to some observational problems (e.g., emission line profile differences and reverberation). This hypothesis will be further investigated in future papers (Korista et al. 1996).

In anticipation of future, more advanced modeling of the broad emission line regions (BLRs) of quasars and active galactic nuclei (AGN), we present here the results of thousands of photoionization calculations that span seven orders of magnitude in hydrogen ionizing flux and particle density. The equivalent widths of 42 of the more prominent quasar emission lines are presented as contours in the particle density – ionizing flux plane, for a typical incident continuum shape, solar chemical abundances, and cloud column density of $N(H) = 10^{23}$ cm^{-2}. Results are similarly given for a small subset of emission lines for two other column densities, five other incident continuum shapes, and a gas metallicity of 5 $Z_{\odot}$. We present this as a foundation for future research, and also as an interpretational aid for the spectroscopic observer.

We describe the calculations and the emission line equivalent width maps in § 2 and conclude in § 3. The digital results of these and many more BEL photoionization grids will be available in electronic form over the Internet. Instructions for electronic retrieval are also given in § 3.

2. The Photoionization Grids

2.1. The Calculations

The line spectrum emitted by individual quasar "clouds" (whatever their nature) depends on a number of parameters, namely, the gas density, the gas column density, the flux and shape of the incident continuum, and the gas chemical abundances. The standard picture is that each observed line is the result of a superposition of line emission from a large number of clouds, each emitting at their thermal width (Davidson & Netzer 1979). The present calculations assume thermal velocity line widths in each cloud. The presence of significant turbulence or streaming motions within the emitting region would have significant effects on the results presented below, and will be the subject of future work. These would mainly act to alter the line escape probabilities (perhaps along preferred directions), thereby reducing the effects of line thermalization at high density and optical depth, and continuum pumping contributions to some emission lines could also become significant.

After choosing a particular chemical abundance (initially solar), incident continuum shape, and cloud hydrogen column density (initially 10^{23} cm^{-2}), we computed an emission line spectrum for each coordinate pair in the gas density – hydrogen-ionizing photon flux plane ($\log n(H)$, $\log \Phi(H)$) using the code Cloudy, version 90.02d (Ferland 1996; Ferland et al. 1996). Constant hydrogen density throughout each cloud was assumed. The results tend to be similar for a similar ionization parameter, defined $U(H) \equiv \Phi(H)/n(H)c$; lines in the gas density – ionizing flux plane with 45° slopes will be of constant $U(H) \times c$. With an origin of $\log n(H) = 7$, $\log \Phi(H) = 17$, the grid was stepped in 0.25 dex increments, and spanned seven orders of magnitude in each direction, for a total of 841 simulations per grid. This should more than cover the parameter space of the broad emission line clouds. Gas densities $> 10^{14}$ cm^{-3} were not considered, since in this regime the calculations are not deemed sufficiently accurate and such clouds are mainly continuum sources (Rees, Netzer, & Ferland 1989).

The chosen form of the incident continuum shape was a combination of a $f_\nu \propto \nu^{-0.5} exp(-h\nu/kT_{cut})$ UV-bump with an X-ray power law of the form $f_\nu \propto \nu^{-1}$ spanning 13.6 eV to 100 keV, appropriate for radio-quiet quasars and AGN (Elvis et al. 1994). We considered two values of the UV-bump cutoff temperature, T_{cut}, such that the energy in the UV-bump peaked at $E_{peak} \approx 22$ eV and 44 eV, corresponding to $\log T_{cut} =$ 5.7, 6.0, respectively. The UV-bump was also cut off in the infrared with a temperature $kT_{IR} = 0.01$ Ryd, corresponding to 9.1 microns. Most of the observed IR continuum is thought to originate in warm dust, far outside the BEL region (Sanders et al. 1989; Barvainis 1990, 1992). Free-free heating from a strong incident IR continuum would have profound effects on the ionization and thermal properties of high density clouds (Ferland

& Persson 1989; Ferland et al. 1992). The UV and X-ray continuum components were combined using a range of UV to X-ray logarithmic spectral slopes of $\alpha_{ox} = -1.2, -1.4$, and -1.6 (note that we prefer the convention $f_\nu \propto \nu^\alpha$). It is defined

$$\frac{f_\nu(2\ keV)}{f_\nu(2500\ \AA)} = 403.3^{\alpha_{ox}}. \tag{1}$$

We plot the incident continua considered here in Figure 1. For our baseline grid we chose the continuum which might typify an average QSO: $E_{peak} = 44$ eV and $\alpha_{ox} = -1.4$. For the hardest value of α_{ox} considered here ($\alpha_{ox} = -1.2$), generally applicable to Seyfert 1 type AGN, the slope of the exponential portion of the UV-bump has a value of roughly -2.3, similar to observed slopes of soft X-ray excesses (e.g., Walter & Fink 1993).

2.2. The Baseline Grid

Our baseline grid assumes solar abundances, a cloud column density of 10^{23} cm^{-2}, and the baseline incident continuum described above. CLOUDY now considers the ionization balance of the first thirty elements; solar abundances are from Grevesse & Anders (1989) and Grevesse & Noels (1993).

H :1.00E+00 He:1.00E-01 Li:2.04E-09 Be:2.63E-11 B :7.59E-10 C :3.55E-04 N :9.33E-05
O :7.41E-04 F :3.02E-08 Ne:1.17E-04 Na:2.06E-06 Mg:3.80E-05 Al:2.95E-06 Si:3.55E-05
P :3.73E-07 S :1.62E-05 Cl:1.88E-07 Ar:3.98E-06 K :1.35E-07 Ca:2.29E-06 Sc:1.58E-09
Ti:1.10E-07 V :1.05E-08 Cr:4.84E-07 Mn:3.42E-07 Fe:3.24E-05 Co:8.32E-08 Ni:1.76E-06
Cu:1.87E-08 Zn:4.52E-08

2.2.1. The Electron Temperature at the Face of the Cloud

Here we illustrate the dependence of the cloud gas temperatures on its position in the gas density – ionizing flux plane. In Figure 2 we plot contours of equal electron temperature at the *face* (T_{face}) of the cloud in this plane, assuming solar chemical abundances and the baseline incident continuum ($E_{peak} = 44$ eV and $\alpha_{ox} = -1.4$). Both parameters will affect the details of this plot, but the trends will remain the same. This temperature is proportional to the ionization parameter, being ~ 7000 K in the lower right corner and increasing slowly at first with increasing ionization parameter until $\log U(H) \sim -1$. Line thermalization is not important at the illuminated face of the cloud, thus its temperature is not strongly dependent upon the gas density at constant $U(H)$. However, other cooling and heating mechanisms do change with density along constant $U(H)$, and this accounts

for the generally gentle bending of the contours with increasing density (the gas is hotter at higher density along constant ionization parameter). In particular, free-free heating becomes very important at high densities, and will depend upon the shape and intensity of the incident infrared continuum. With increasing $U(H)$ the temperature at the face of the cloud climbs more rapidly than at low $U(H)$, reaching 10^5 K at $\log U(H) \sim 1$. Gas near this temperature is cooling mainly via O VI $\lambda1034$ and then Ne VIII $\lambda774$, with a diminishing contribution from C IV $\lambda1549$. Once these ions begin to disappear, the gas can no longer cool efficiently; the temperature contours become very dense just beyond $\log U(H) \sim 1$, and the gas temperature jumps from $\sim 10^5$ K to $\sim 10^6$ K; this is the well known thermal instability gap (see for instance Krolik, McKee, & Tarter 1981; Reynolds & Fabian 1995). It is this feature which will be particularly sensitive to continuum shape and chemical abundances assumed. For example, the band of dense contours lying between $\log T = 5$ and 6, representing the instability gap, moves to lower ionization parameter for harder continua. This thermally unstable gas or gas just a bit cooler (and thermally stable) may be present near the central engines of AGN. Gas with temperatures of $1 - 2 \times 10^5$ K and column densities of $\sim 10^{22}$ cm^{-2} has been observed in AGN soft X-ray spectra in the form of "warm absorbers" (Fabian et al. 1994; George, Turner, & Netzer 1995). The identifications of significant Ne VIII $\lambda774$ emission in some QSO spectra (Hamann et al. 1995; Hamann, Zuo, & Tytler 1995) indicates the presence of the same gas in higher column density clouds ($> 10^{23}$ cm^{-2}). This "warm" phase gas warrants further study. At still larger ionization parameters the gas temperature climbs toward the Compton temperature for the assumed incident continuum (4.7×10^6 K). The temperature again becomes insensitive to further increases in the ionization parameter, as Compton heating and cooling are in balance.

2.2.2. Emission Line Equivalent Widths

In Figures 3a – 3g we present contours of logarithmic equivalent width of 42 quasar emission lines in the $\log n(H)$ – $\log \Phi(H)$ plane. The equivalent width (W_λ in Å) is measured relative to the incident continuum at 1216 Å for full source coverage, and is a measure of the cloud's ability to reprocess the continuum into the emission line. Here, full source coverage means that the "sky", from the perspective of the continuum source, is completely covered by clouds: $f_c \equiv 1$. Results for cloud covering fractions less than 1 may be obtained through a simple rescaling. The W_λ distributions are laid out in order of increasing wavelength of the emission line, and the minimum contour plotted has a value of 1 Å in every case. Most of the first seven far-UV emission lines have rarely, if ever, been reported, and are plotted in light of the recent *Hubble Space Telescope* spectra of $z \sim 1$ quasars. Baldwin et al. (1995) discussed some of the details of the W_λ distributions, and we

elaborate on some of their discussion below.

2.2.3. The Collisionally-Excited Metal Lines

Collisionally excited lines such as C IV $\lambda1549$ (Figure 3d) generally show a band of efficient reprocessing running at constant $U(H) \equiv \Phi(H)/n(H)c$ along the *center* of a diagonal ridge from high $\Phi(H)$ and $n(H)$, to low $\Phi(H)$ and $n(H)$. For C IV $\lambda1549$ this ridge corresponds to a $\log U(H) \approx -1.5$. The gentle decrease in W_λ along the ridge at constant $U(H)$ is the result of thermalization, described further below. The W_λ decreases sharply when moving orthogonal to the ridge because $U(H)$ is either too low (lower right) or too high (upper left) to produce the line efficiently. For a column density of 10^{23} cm^{-2}, clouds with $\log U(H) \gtrsim 0.5$ are optically thin to He$^+$ ionizing photons ($h\nu \gtrsim 54$ eV) and so reprocess little of the incident continuum. C IV $\lambda1549$ can be contrasted with a lower ionization line such as C III $\lambda977$ (Figure 3b), whose peak W_λ is shifted to lower $\log U(H)$ (≈ -2.25), or to the high ionization O VI $\lambda1034$ (Figure 3b), shifted to higher $\log U(H)$ (≈ 0).

A few effects modify the ridge of peak emission efficiency. The high ionization potential, high excitation energy of the Ne VIII $\lambda774$ emission line along with the finite cloud column density together conspire to make its ridge of reprocessing efficiency very narrow in Figure 3a. The required ionization parameter is large, $\log U(H) > 0.5$, and clouds with column densities of 10^{23} cm^{-2} are becoming optically thin to He$^+$ ionizing photons; this line is nearly fully formed within such clouds (see Hamann et al. 1995). However, to fully form the peak ridge in the W_λ distribution of Ne VIII $\lambda774$ in the density – ionizing flux plane requires larger column densities and ionization parameters ($\log N(H) \sim 10^{24}$ cm^{-2}, $\log U(H) \sim 1$). Because of their narrowness, the W_λ(Ne VIII) contours are best viewed by looking obliquely along the diagonal ridge. This effect will also be important to Mg X $\lambda615$, and to a lesser degree O VI $\lambda1034$, at this cloud column density.

The second effect is thermalization. This is most readily seen when comparing an intercombination line with a resonance line of the same ion. The classic example is C III $\lambda977$ and C III] $\lambda1909$ (Figures 3b and 3e). While their ridges of peak W_λ have nearly the same ionization parameter ($\log U(H) \approx -2.5$), the intercombination line begins to thermalize at densities $\lesssim 10^{9.5}$ cm^{-3}, while the resonance line does not begin to thermalize until the density has reached $\gtrsim 10^{12}$ cm^{-3}. A smaller gas density at the same $U(H)$ means smaller ionizing fluxes, corresponding to larger distances from an isotropically emitting continuum source. These two lines may be emitted in very different clouds. Thermalization at large optical depth is the reason for the peculiar W_λ distributions in lines such as O I

λ1304 and Mg II λ2798 (Figures 3c and 3f). The O I line is also extremely sensitive to the presence of the hydrogen ionization front within the cloud; this accounts for the "noise" in the contours along its upper boundary. Emission lines which continue to become stronger at densities $> 10^{11}$ cm^{-3}, as the traditional coolants become thermalized, are those which lie in the Lyman continuum, C III λ977, N III λ990, C III* λ1176, N V λ1240, C II λ1335, Si IV λ1397, Al III λ1859, and Mg II λ2798. In the optical, Ca II (H & K and the near-IR triplet), and Na I λ5895, become increasingly strong at very high densities. The strengths of these lines should be important indicators of the importance of ionized high density clouds in the BLR.

One other effect is readily apparent in the W_λ distributions of those lines formed in the He$^+$ zone: in the gas density – ionizing flux plane a secondary, more localized ridge of high efficiency forms at larger $U(H)$ for gas densities $\gtrsim 10^9$ cm^{-3}. This effect is seen as secondary peaks in the W_λ(N III] λ1750) and W_λ(C III] λ1909) located near the coordinates (10.00,19.75; Figure 3e) and (9.50,19.50; Figure 3e), respectively, or as bulges in the W_λ distributions of C II λ1335, C III λ977, N III λ990, O III] λ1663, and Si IV λ1397. For the relevant ionization parameters, an extended H$^+$ – He$^+$ Strömgren zone forms in these clouds, increasing the relative emitting volumes for the aforementioned lines. This line emission eventually thermalizes at higher flux levels at constant $U(H)$ (i.e., for $\log n(H) \gtrsim 10^{10-11}$ cm^{-3}). This effect will be more important for higher column density clouds. Note that considerable overlap in the efficient emission of C III λ977 and C III] λ1909 occurs for clouds whose properties lie in this region in the gas density – ionizing flux plane, in contrast to the ridge of primary efficiency at lower $U(H)$, as discussed above.

It should be noted by the reader that dielectronic recombination contributes significantly to the emission of several high excitation lines, such as C II λ1335, C III λ977, C III* λ1176, N III λ990, N IV λ764, O III λ835, and O V λ630. This contribution tends to be more important for the lower ionization lines, because the collisional rates are small due to the Boltzmann factor. The recombination rates were taken from Nussbaumer & Storey (1983). The recombination contribution is also very important in the "bulge" and "secondary peak" regions in the gas density – ionizing flux plane for several of the lines which have these features, just described above. This is likely due to the fact that these lines at these positions in the gas density – ionizing flux plane are forming at larger depths in the cloud, where the temperatures are lower.

Finally, we do not investigate here the complicated emission from Fe II. The present version of CLOUDY predicts the heating and cooling contributions from Fe II based upon a modified version of the Wills, Netzer, & Wills (1985) model, and will be discussed elsewhere (Hamann et al. 1996). More advanced calculations of the emission of Fe II and its role in the

thermal balance of BEL clouds will be the subject of future work (see Verner et al. 1995).

2.2.4. The Hydrogen and Helium Lines

Lines of H^o, He^o, and He^+ are largely produced via recombination and emitted over a wider area on the gas density – ionizing flux plane, including the low $\Phi(H)$ – high $n(H)$ regions. This is because these ions still exist under these conditions. At sufficiently high ionization parameter for the given cloud column density, the H, He, and He^+ ionization fronts reach the backs of the clouds causing the dramatic declines in W_λ of the Balmer lines, He I λ5876, and He II λ4686 (see Figures 3f, 3g). These same lines have their peak efficiencies at high densities ($\log n(H) \gtrsim 12$), but different ionizing photon fluxes. Note that in this high density regime, substantial emission arises from collisional excitation. A feature common to most of the hydrogen and helium emission lines is saturation at high continuum fluxes. In contrast to the excited state transitions of H and He, Lyα λ1216 thermalizes at high density as well as high flux (Figure 3c; see also Lyβ an Lyγ in Figure 3b). Another common feature is that they weaken in the direction of very high density and very low flux (lower right corners) where either the ionized fractions of the H, He ions are becoming very small or the temperature is becoming too low to support the collisional excitation of the neutrals. Note that the Balmer and Paschen continua "W_λ" distributions (Figures 3f and 3g) are the integrated fluxes from these diffuse continua ratioed to the incident continuum flux-density at 1216 Å. Finally we note that the assumed ionizing spectrum predicts a W_λ(Lyα) ≈ 1089Å (3.04 in the logarithm) for full coverage by an optically thick cloud if all hydrogen ionizing photons are converted into Lyα. Compare this with its computed W_λ contours in Figure 3c. Thermalization and destruction via background continuum opacities (Balmer continuum, Fe II, etc) act to diminish this conversion efficiency (Davidson & Netzer 1979; Shields & Ferland 1993).

2.3. Other Cloud Column Densities

For solar abundances and the same incident continuum shape, Figures 4a – 4c show the contours of $\log W_\lambda$ for six selected emission lines for cloud column densities of 10^{22} cm^{-2}, 10^{23} cm^{-2}, and 10^{24} cm^{-2}, respectively. A comparison between the two extremes, Figures 4a and 4c, shows the expected results. For the hydrogen and helium recombination lines (left panels), the ionization parameter which fully ionizes the clouds is simply proportional to the cloud column density: $N(H^+) \approx 10^{23.1} \times U(H)$ cm^{-2}.

This region of dramatic decline in W_λ also shifts to lower $U(H)$ with a decrease in the cloud column density for the collisionally excited metal lines (right panels). The high ionization lines, for example O VI λ1034, are affected in an additional way: the position of the ridge top shifts to lower $U(H)$ for smaller column densities in order for a sufficient volume of O^{+5} to exist within the cloud. The combined effects of these act to first diminish the lines' ridge W_λ areas in the gas density – ionizing flux plane, and eventually to reduce their peak contour values as the cloud column density is decreased. Thus, for a distribution in cloud column densities the highest ionization lines are emitted most efficiently in the highest column density clouds. As an illustration of this we note that efficient emitters of O VI λ1034 are mainly optically thick clouds whose column densities are 10^{24} cm^{-2}, a roughly even mixture of optically thick/thin clouds whose column densities are 10^{23} cm^{-2}, and mainly optically thin clouds whose column densities are 10^{22} cm^{-2}. This can be seen by comparing the ridge tops of this line for the three column densities to a line representing the ionization parameter at which the cloud becomes optically thin to hydrogen ionizing photons for that column density.

Finally, the W_λ distributions in the low ionization lines, such as Mg II λ2798, primarily formed in a partially ionized hydrogen zone (PIZ), are not strongly affected at significant W_λ until the cloud column density drops substantially below 10^{22} cm^{-2}. This is also true of the hydrogen and helium emission lines at high density.

2.4. Other Ionizing Continuum Shapes

In Figures 5a – 5e we show the W_λ distributions for the same six emission lines for solar abundances, a cloud column density of 10^{23} cm^{-2}, and five other incident continuum shapes (see Figure 1). The results for the baseline continuum are shown in Figure 4b. Moving from the hardest (Figure 5a) to the softest (Figure 5e) continuum, the major change for most emission lines is that the value of the peak equivalent width diminishes, and/or the peak contours shrink in area in the gas density – ionizing flux plane. When comparing the results between the two types of UV-bumps, about 0.15 dex of the changes in the peak line equivalent widths are due to the fact that for the same number of hydrogen ionizing photons, a softer UV bump will have more flux in the observed UV continuum upon which the lines lie than a harder one (see Figure 1). The remaining differences are due to the quantity of photons at relevant energies to produce and excite the ions. Some line ratios, such as Lyα/He II, are expected to be sensitive mainly to the hardness of the UV-bump (n_{ph}(912 Å)/n_{ph}(228 Å)), while those involving the strong metal line coolants (e.g., Lyα/C IV and C IV/He II) should be dependent on both the hardness of the UV-bump

and α_{ox}. It is also the case for many of the metal lines that the upper boundary on $U(H)$ for significant reprocessing efficiency shifts to lower $U(H)$ for harder continua. This is because continua with larger ratios of soft X-ray to 912 Å photons are more efficient in stripping electrons from the ionized metals. This effect is especially apparent in lines like O VI λ1034 (compare Figures 5a and 5e). Note, however, that the contours of lines formed in a PIZ, like Mg II λ2798, become larger in the directions of larger $U(H)$ for harder continua, because the volume of a PIZ within a cloud becomes larger at constant $U(H)$ for harder continua (compare Figures 5a and 5e).

2.5. Z= 5 $Z_\odot$

Using the baseline incident continuum shape and a cloud column density of $N(H) = 10^{23}$ cm^{-2}, we computed another grid assuming a metallicity of 5 $Z_\odot$, similar to that deduced for some high-redshift quasars (Hamann & Ferland 1993; Ferland et al. 1996). We used the chemical abundance set derived by Hamann & Ferland for their model M5a and Z = 5 $Z_\odot$ (see Hamann & Ferland and Ferland et al.). The abundances, by number relative to hydrogen, are:

H :1.00E+00 He:1.27E-01 Li:1.19E-08 Be:1.54E-10 B :4.44E-09 C :8.06E-04 N :9.61E-04
O :5.18E-03 F :1.95E-07 Ne:7.55E-04 Na:1.36E-05 Mg:2.51E-04 Al:1.93E-05 Si:2.29E-04
P :2.41E-06 S :1.06E-04 Cl:1.21E-06 Ar:2.57E-05 K :8.72E-07 Ca:1.42E-05 Sc:2.24E-09
Ti:1.56E-07 V :1.49E-08 Cr:6.87E-07 Mn:4.85E-07 Fe:4.60E-05 Co:1.18E-07 Ni:2.50E-06
Cu:2.65E-08 Zn:6.41E-08

The W_λ distributions for the same six selected emission lines are shown in Figure 6. Comparing these results to those in Figure 4b (same incident continuum and cloud column density, but solar abundances), one can see several important differences. First, the hydrogen and helium lines' peak W_λ values are diminished at a metallicity of 5 $Z_\odot$ by a modest amount (0.1 – 0.2 dex) compared to solar. This is because the metals become important opacity sources with increasing metallicity, replacing to a significant degree, hydrogen and helium. Second, the peak values of the O VI λ1034 and C IV λ1549 W_λ distributions are both diminished by about 0.4 dex. With increasing metallicity, Z, the nitrogen abundance scales like Z^2 (Hamann & Ferland 1993), and the cooling from carbon and oxygen is shifting over to nitrogen. In addition the strong metal opacity and accompanying lower electron temperatures shrink the emitting volumes of especially the higher ionization emission lines. See Ferland et al. (1996) for specific predictions regarding N V, He II and Z-dependent behavior.

2.6. Anisotropic Line Emission

Davidson and Netzer (1979) and Ferland et al. (1992) discussed the anisotropic line emission from clouds. O'Brien et al. (1994) demonstrated the effects of this "line beaming" on the response functions and line profiles of the emission lines. In general, strong resonance lines, as well as optically thick excited state lines (e.g., Hβ λ4861, He II λ1640) will generally preferentially escape out the front sides of the clouds (i.e., the side facing the incident continuum). The conditions which lead to significant line beaming will differ for individual lines, depending mainly on the ionization and temperature structure. For example, Lyα becomes fully anisotropic with the formation of a hydrogen ionization front within the cloud, but nearly isotropic in clouds which are optically thin to hydrogen ionizing photons. Most other lines require more specific conditions and are not so "binary" in their inward/outward emission. In the case of C IV λ1549, the degree of the anisotropy is approximately proportional to the ionization parameter. This is because the size of the ionized portion of the cloud, and thus the C^{3+} column density, is proportional to $U(H)$. This line also becomes more anisotropic with increasing gas density at constant ionization parameter, i.e., in the direction of thermalization. The two effects result in anisotropic emission for the following reason. Because the peak of the line source function within a cloud does not coincide with the position of the peak ion fraction (the former lies closer to the front face of the cloud where the temperature is higher), the line is beamed toward the continuum source. In general harder continua produce C IV (and other lines) more isothermally in this respect, and the line emission will be more isotropic than in clouds which are illuminated by softer continua.

In Figure 7, we show contours of constant logarithmic ratios of F_{in}/F_{total} for C IV λ1549, assuming the baseline continuum, solar abundances, and cloud column densities of 10^{23} cm^{-2}. The radiative transfer computations assume plane parallel slab clouds; the actual line beaming function may be more complicated depending on the cloud geometry, non-radial transfer, and other effects. A comparison with Figure 4b shows that clouds should emit C IV anisotropically where its strength is significant. Low density clouds which are becoming fully ionized in hydrogen are nearly isotropic emitters (lower left corner), but are anisotropic emitters at larger gas densities (moving toward the upper right corner). Clouds optically thick to hydrogen ionizing photons beam C IV preferentially inward, with the beaming factor increasing as the line becomes thermalized. The steep gradient in the inward/total ratio along the upper diagonal boundary roughly coincides with the clouds becoming optically thin to 54 eV photons, and thus with the steep decline in the W_λ(C IV). This boundary shifts with cloud column density; little else changes with changing column density in Figure 7. Other incident continuum shapes, different chemical abundances, and the presence of non-thermal motions would change the nature of the line beaming

significantly, however.

3. Conclusions

We have presented these grids to quantitatively show the general dependence of the emission spectrum from individual BLR gas clouds to changes in the most important input parameters. While most of these trends will seem obvious in a qualitative sense, we hope that the diagrams presented here will help future researchers to navigate more easily through the $\Phi(H), n(H), N(H)$, continuum-shape, metallicity parameter space.

The difference between the logarithmic equivalent width contour plots for two different lines will be logarithmic contours of the line intensity ratio, which is of considerable interest for analyzing observational data. These grids should also prove valuable to the detailed modeling of broad line regions, since all such models must include emissivity from a distribution in cloud properties.

We have chosen not to present intensity-ratio contour plots here (a subject of future work), but rather to make the numerical data from the equivalent width grids easily available over the Internet. These data are accessible via the Cloudy home page (currently "http://www.pa.uky.edu/∼gary/cloudy/"). A readme file describes the data files and will log their updates. The data base contains the information, as plotted in Figure 3, for over 100 emission lines and diffuse continua in a 3 column ascii format file for each emission line: $\log n(H), \log \Phi(H), W_{\lambda 1216}/1216$. Information on how to convert a line's $W_{\lambda 1216}/1216$ to it's surface flux (useful for detailed modeling of the BLR) for a given incident continuum shape are provided. All of these are available for a variety of incident continuum shapes, many cloud column densities, a few sets of gas abundances, and other parameters.

We thank the referee, Fred Hamann, for his helpful comments and suggestions. This work was supported by the NSF (AST 93-19034), NASA (NAGW-3315, NAG-3223), and STScI grant GO-2306.

REFERENCES

Baldwin, J.A., Ferland, G.J., Korista, K.T., & Verner, D. 1995, ApJ, 455, L119

Barvainis, R. 1990, ApJ, 353, 419

Barvainis, R. 1992, ApJ, 400, 502

Clavel, J., et al. 1991, ApJ, 366, 64

Corbin, M.R. 1990, ApJ, 357, 346

Davidson, K. 1977, ApJ, 218, 20

Davidson, K., & Netzer, H. 1979, Rep. Prog. in Physics 51, 715

Elvis, M., et al. 1994, ApJS, 95, 1

Espey, B.R., Carswell, R.F., Bailey, J.A., Smith, M.G., & Ward, M.J. 1989, ApJ, 342, 666

Fabian, A.C., et al. 1994, PASJ, 46, L59

Ferland, G.J., 1996, Hazy, a Brief Introduction to Cloudy, University of Kentucky Physics Department Internal Report

Ferland, G.J., Korista, K.T., Verner, D.A., Ferguson, J.W., Kingdon, J., & Verner, E.M. 1996, PASP, in preparation

Ferland, G.J., Baldwin, J.A., Korista, K.T., Hamann, F., Carswell, R.F., Phillips, M.M., Wilkes, B.J., & Williams, R.E. 1996, ApJ, 461, 683

Ferland, G.J., & Persson, S.E. 1989, ApJ, 347, 656

Ferland, G.J., Peterson, B.M., Horne, K., Welsh, W.F., & Nahar, S.N. 1992, ApJ, 387, 95

Gaskell, C.M. 1982, ApJ, 263, 79

George, I.M., Turner, T.J., & Netzer, H. 1995, ApJ, 438, L67

Goad, M.R., O'Brien, P.T., & Gondhalekar, P.M. 1993, MNRAS, 263, 149

Grevesse, N., & Anders, E. 1989, in AIP Conf. Proc. 183, Cosmic Abundances of Matter, ed. C.J. Waddington (New York: AIP), 1

Grevesse, N., & Noels, A., 1993, in Origin and Evolution of the Elements, ed. N. Prantzos, E. Vangioni-Flam, & M. Casse (Cambridge Univ. Press), p. 15

Hamann, F., et al. 1996, in preparation

Hamann, F., & Ferland, G.J. 1993, ApJ, 418, 11

Hamann, F., Shields, J.C., Ferland, G.J., & Korista, K.T. 1995, ApJ, 454, 688

Hamann, F., Zuo, L, & Tytler, D. 1995, ApJ, 444, L69

Korista, K.T., et al. 1996, in preparation

Krolik, J.H., Horne, K., Kallman, T.R., Malkan, M.A., Edelson, R.A., & Kriss G.A. 1991, ApJ, 371, 541

Krolik, J.H., McKee, C.F., & Tarter, C.B. 1981, ApJ, 249, 422

Kwan, J., & Krolik, J. 1981, ApJ, 250, 478

Nussbaumer, H., & Storey, P.J. 1983, A&A, 126, 75

O'Brien, P.T., Goad, M.R., & Gondhalekar, P.M. 1994, MNRAS, 268, 845

O'Brien, P.T., Goad, M.R., & Gondhalekar, P.M. 1995, MNRAS, 275, 1125

Peterson, B.M. 1993, PASP, 105, 247

Rees, M.J., Netzer, H., & Ferland, G.J. 1989, ApJ, 347, 640

Reynolds, C.S., & Fabian, A.C. 1995, MNRAS, 273, 1167

Sanders, D.B., et al. 1989, ApJ, 347, 29

Shields, J.C., & Ferland, G.J. 1993, ApJ, 402, 425

Verner, E.M., Ferland, G.J., Korista, K.T., & Verner, D.A. 1995, BAAS, 27, 840

Walter, R., & Fink, H.H. 1993, A&A, 274, 105

Walter, R., Orr, A., Courvoisier, T.J.-L., Fink, H.H., Makino, F., Otani, C., & Wamsteker, W. 1994, A&A, 285, 119

Wilkes, B.J. 1984, MNRAS, 207, 73

Wilkes, B.J., Tananbaum, H., Worrall, D.M., Avni, Y., Oey, M.S., & Flanagan, J. 1994, ApJS, 92, 53

Wills, B., Netzer, H., & Wills, D. 1985, ApJ, 288, 94

Figure Captions

Fig. 1.— The continuum spectral energy distributions considered in this paper. The UV-bump peaks at $E_{peak} \approx 44$ eV for the solid lines and at $E_{peak} \approx 22$ eV for the dashed lines. Three separate values of α_{ox} were considered, top to bottom: $-1.2, -1.4, -1.6$. All continua plotted here have the same flux in hydrogen ionizing photons.

Fig. 2.— Contours of constant logarithm of the electron temperature at the front face (first zone) of the cloud as a function of hydrogen ionizing photon flux and hydrogen density. The baseline incident continuum (a UV-bump that peaks near 44 eV and an $\alpha_{ox} = -1.40$) and solar chemical abundances were assumed. The contours of 10^4 K and $10^6.6$ K are both labeled and increase monotonically from the lower right corner to the upper left where the Compton temperature for this continuum is reached (4.7×10^6 K). The solid contours are decades and the dotted are 0.1 dex increments.

Fig. 3a.— Contours of $\log W_\lambda$ for six emission lines for the baseline grid is shown as a function of the hydrogen density and flux of hydrogen ionizing photons. The chemical abundances are solar, the cloud column density is 10^{23} cm^{-2}, the continuum spectral energy distribution has a UV-bump that peaks near 44 eV and an $\alpha_{ox} = -1.40$. Line strengths are expressed as logarithmic equivalent widths referenced to the incident continuum at 1216 Å for full source coverage. In this and in all figures that follow, the smallest decade contoured is 1 Å, each solid line is 1 dex, and dotted lines represent 0.2 dex steps. In each case the peak in the equivalent width distribution lies beneath the center of a solid triangle. The contours generally decrease monotonically from the peak to the 1 Å contour. See text for further details. The solid star is a reference point marking the "standard BLR" parameters discussed by Davidson and Netzer (1979).

Fig. 3b.— Same as Figure 3a for other emission lines.

Fig. 3c.— Same as Figure 3a for other emission lines.

Fig. 3d.— Same as Figure 3a for other emission lines.

Fig. 3e.— Same as Figure 3a for other emission lines.

Fig. 3f.— Same as Figure 3a for other emission lines.

Fig. 3g.— Same as Figure 3a for other emission lines.

Fig. 4a.— Same as Figure 3 for a column density of 10^{22} cm^{-2} and a selection of six emission lines.

Fig. 4b.— Same as Figure 3 for a column density of 10^{23} cm^{-2} and a selection of six

emission lines.

Fig. 4c.— Same as Figure 3 for a column density of 10^{24} cm^{-2} and a selection of six emission lines.

Fig. 5a.— Same as Figure 4b for a continuum spectral energy distribution whose UV-bump peaks at 44 eV and has an $\alpha_{ox} = -1.20$.

Fig. 5b.— Same as Figure 4b for a continuum spectral energy distribution whose UV-bump peaks at 22 eV and has an $\alpha_{ox} = -1.20$.

Fig. 5c.— Same as Figure 4b for a continuum spectral energy distribution whose UV-bump peaks at 22 eV and has an $\alpha_{ox} = -1.40$.

Fig. 5d.— Same as Figure 4b for a continuum spectral energy distribution whose UV-bump peaks at 44 eV and has an $\alpha_{ox} = -1.60$.

Fig. 5e.— Same as Figure 4b for a continuum spectral energy distribution whose UV-bump peaks at 22 eV and has an $\alpha_{ox} = -1.60$.

Fig. 6.— Same as Figure 4b for enhanced metal abundances. A metallicity of Z= 5 was assumed, using the abundance grids of Hamann & Ferland (1993).

Fig. 7.—Contours of logarithmic inward to total emission line flux ratios for C IV λ1549, assuming the baseline grid parameters. The most important contours are labeled, with −0.30 designating isotropic emission (inward/outward flux ratio= 1.0), and −0.05 designating clouds emitting C IV most anisotropically. The step size for the contours is 0.05 dex. See text for details.

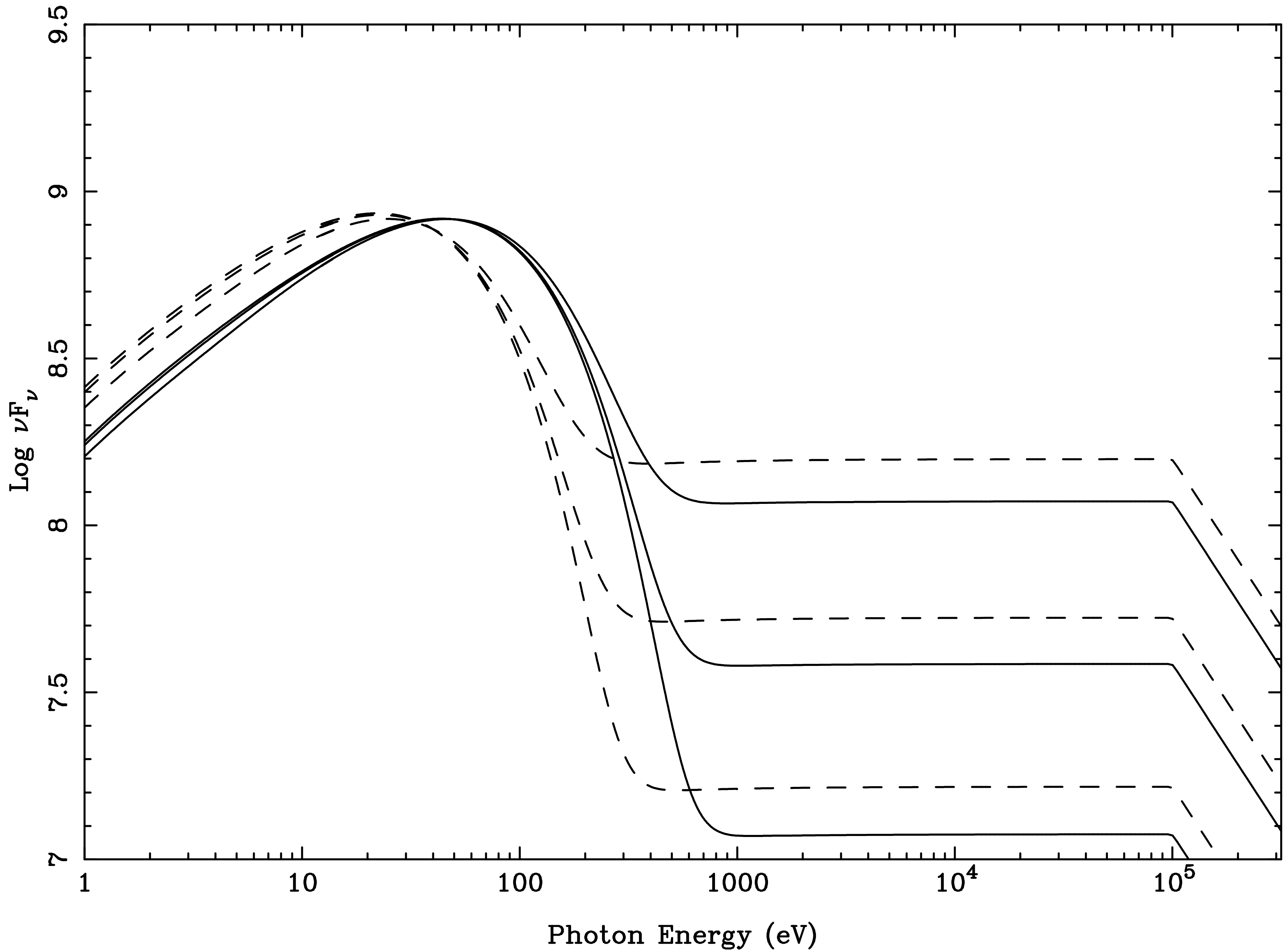
Log νF_ν
9.5
9
8.5
8
7.5
7
1
10
100
1000
10^4
10^5
Photon Energy (eV)

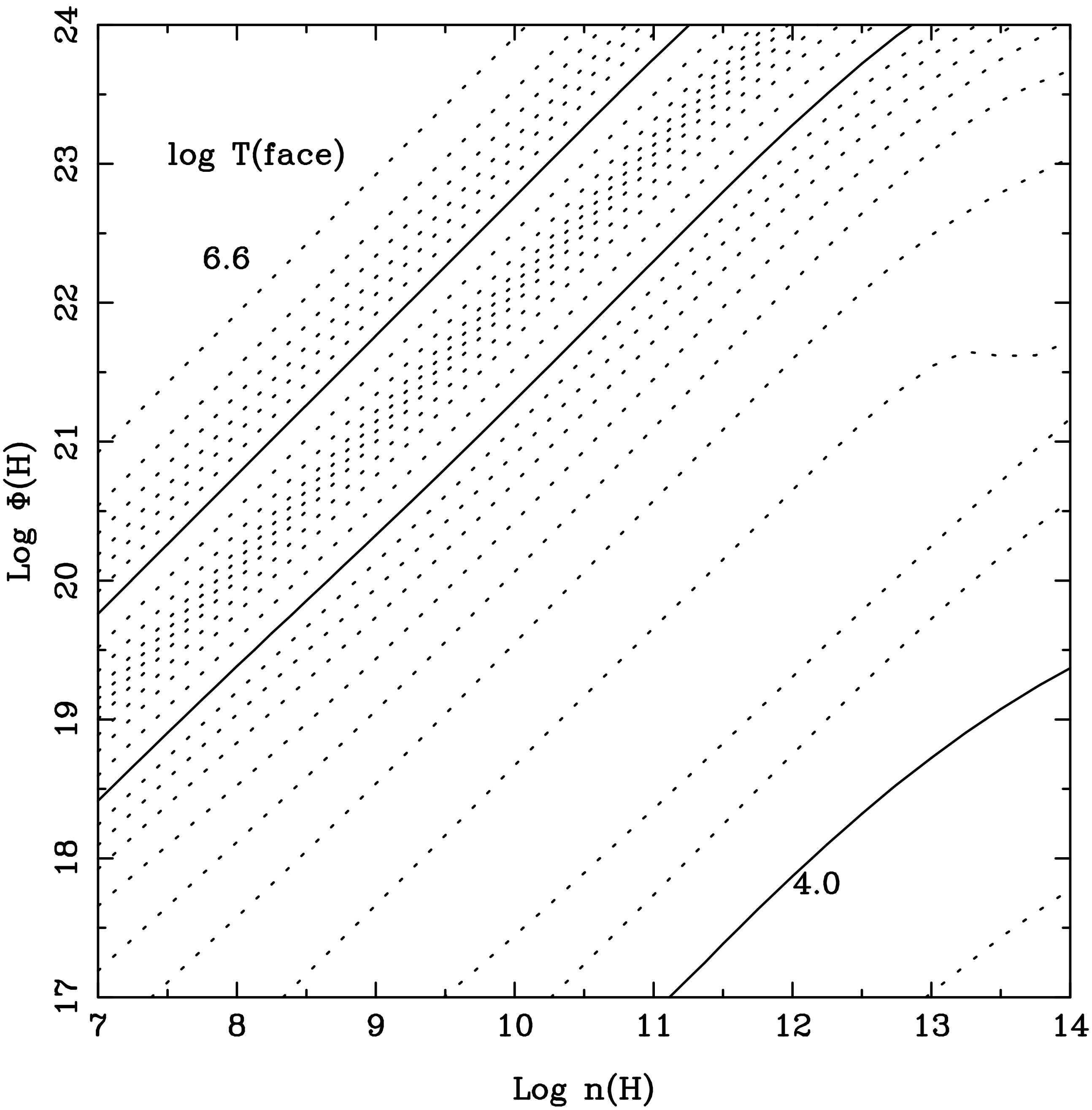

korista 19-Nov-1996 10:03

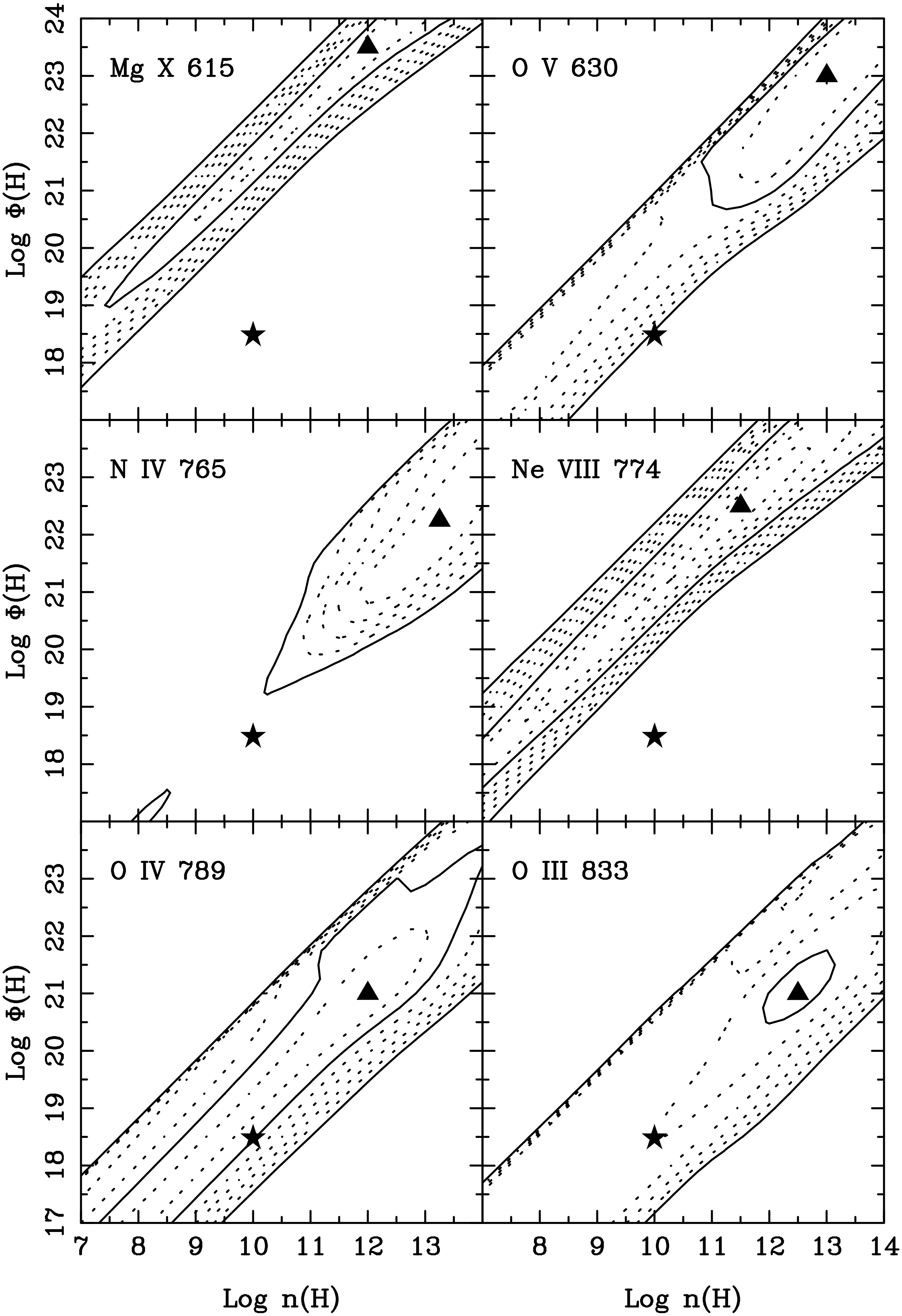

korista 19–Nov–1996 10:08

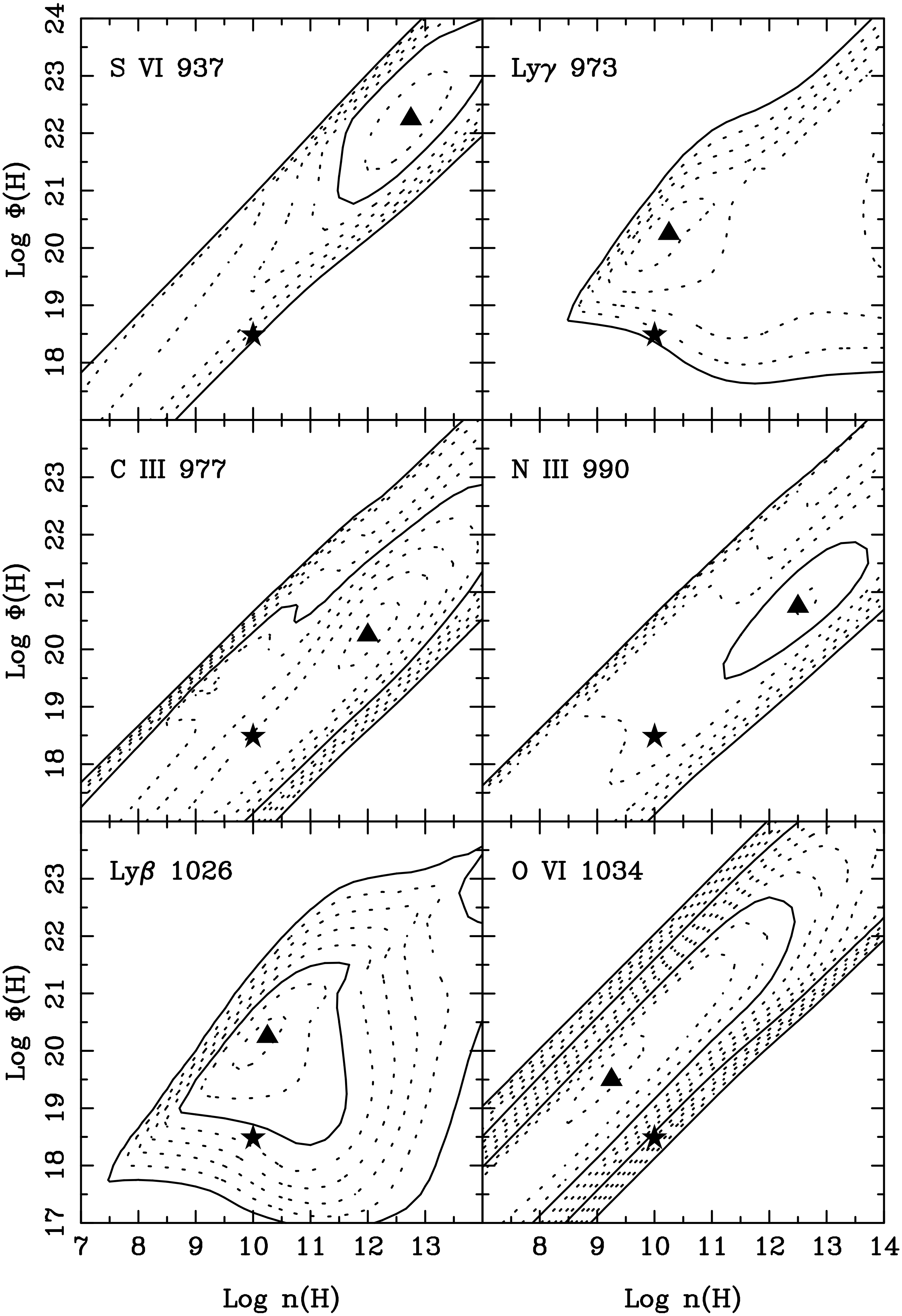

korista 19−Nov−1996 10:12

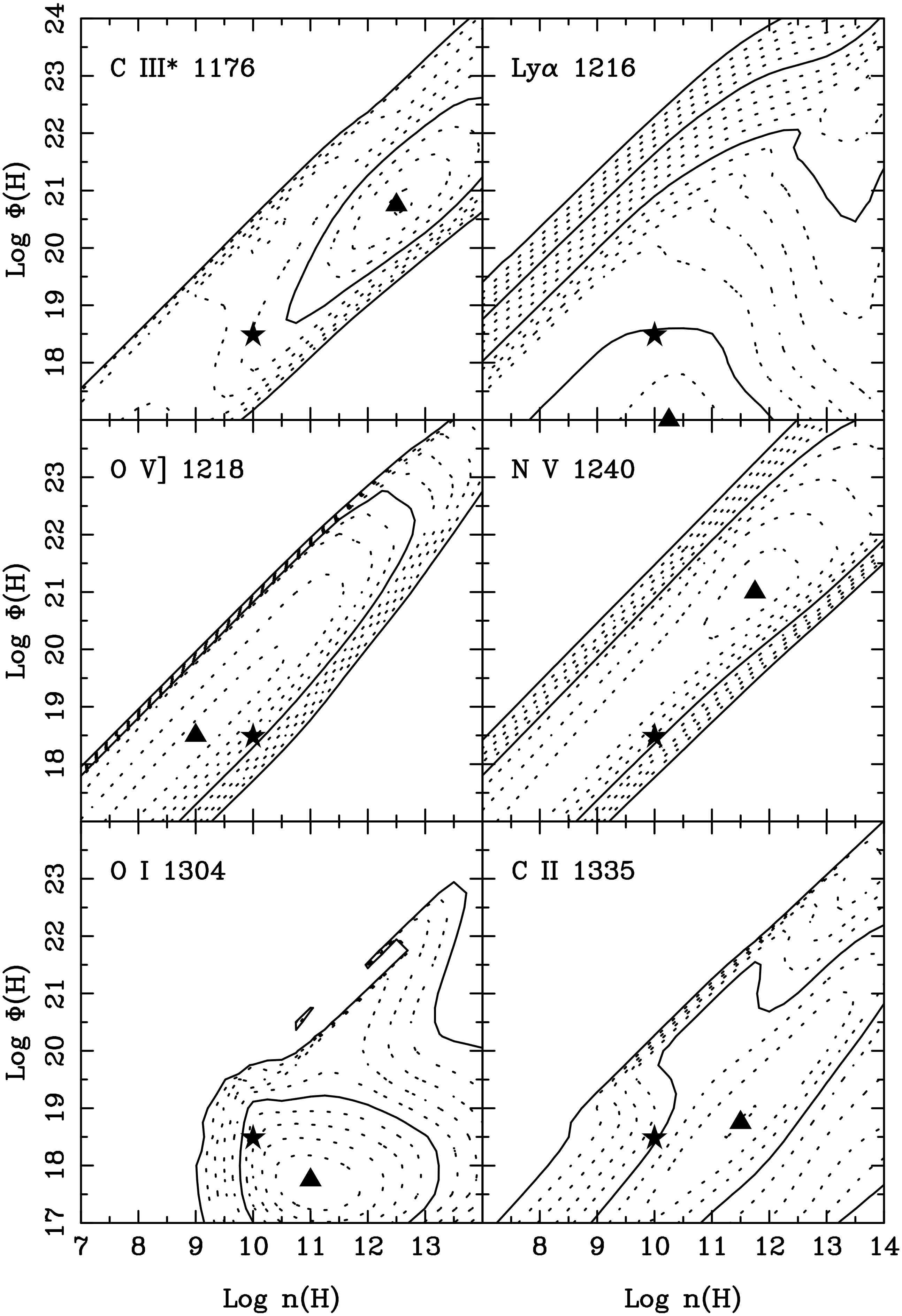

korista 19-Nov-1996 10:15

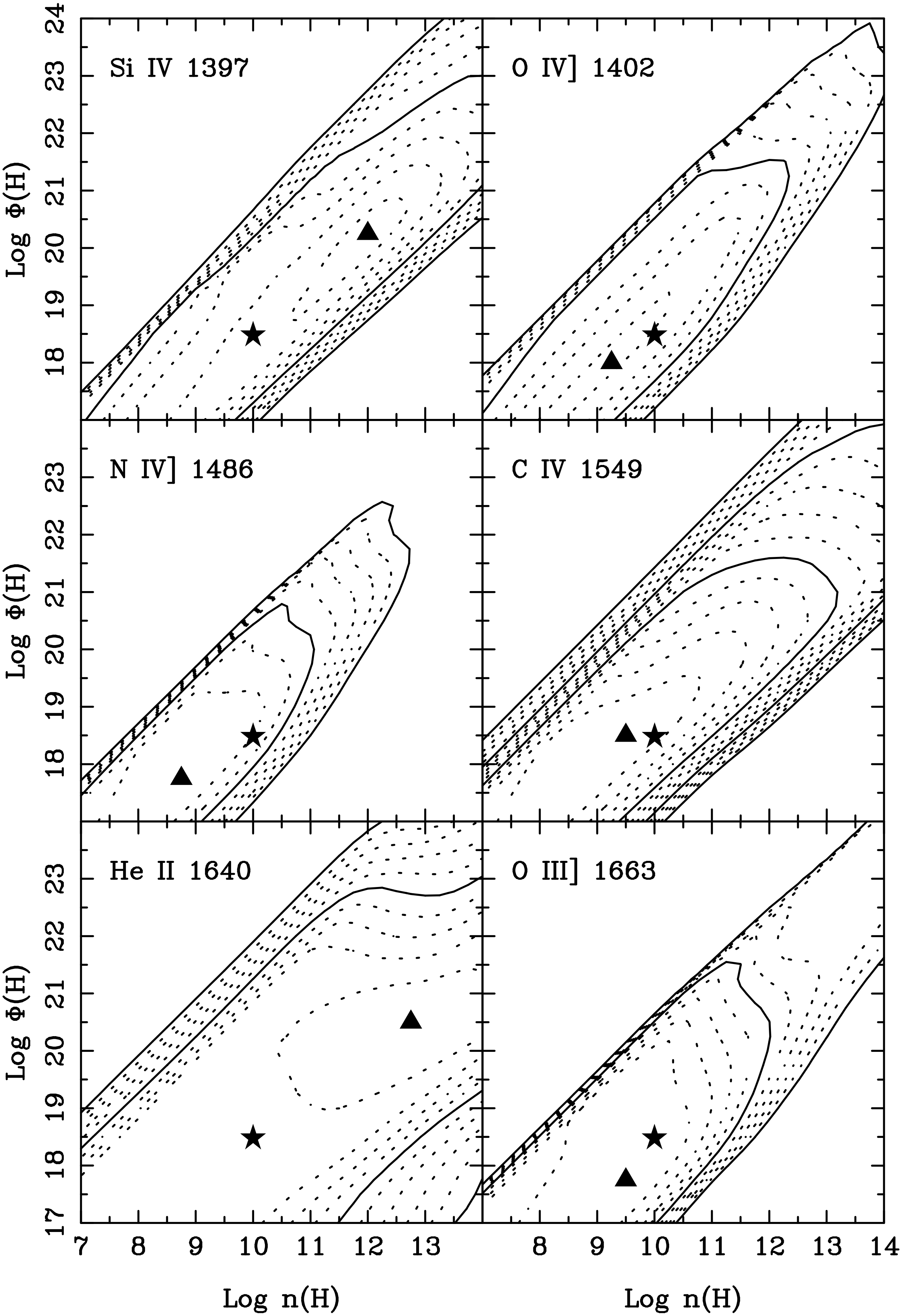

korista 19-Nov-1996 10:26

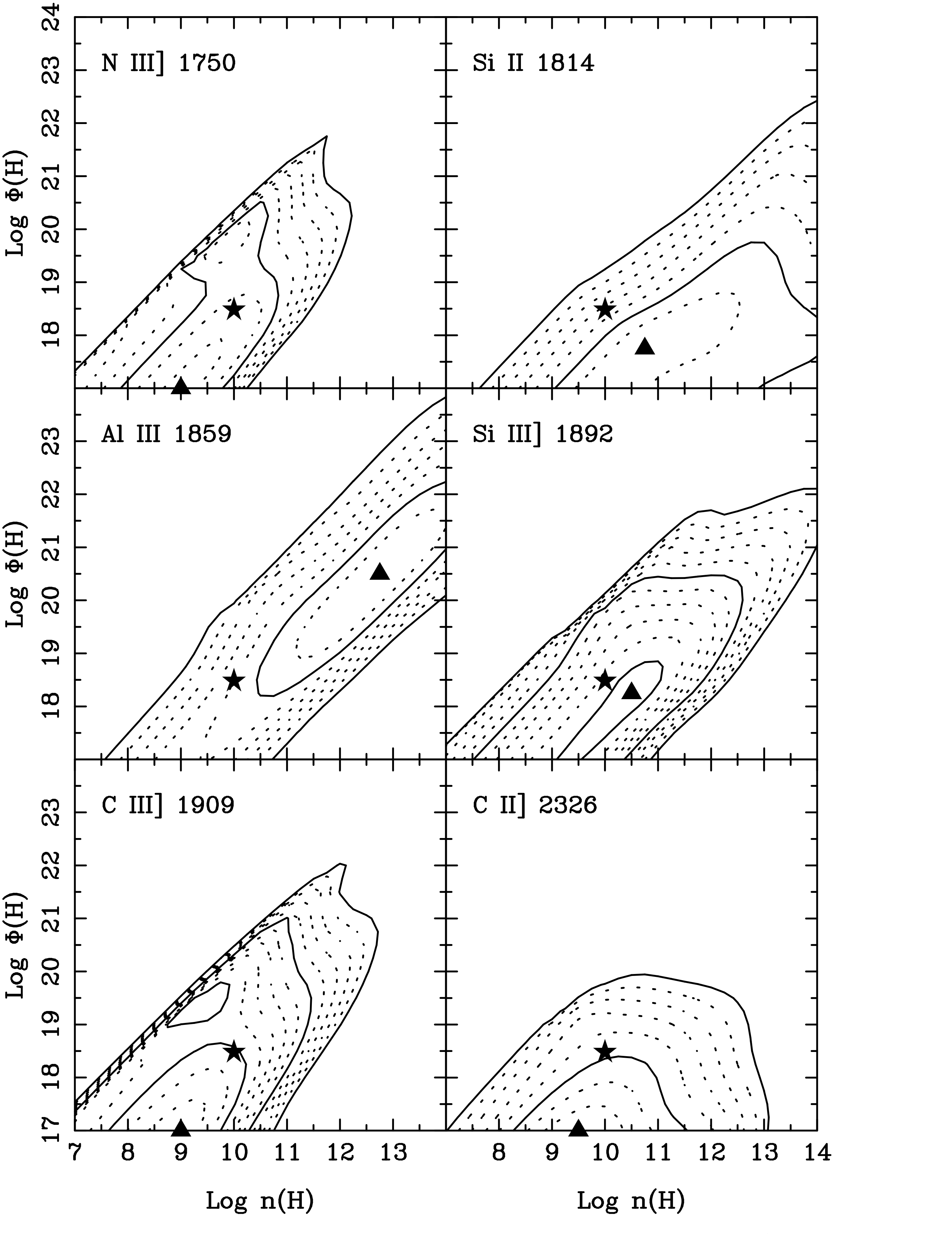

N III] 1750
Si II 1814
Al III 1859
Si III] 1892
C III] 1909
C II] 2326
Log Φ(H)
Log n(H)
korista 19-Nov-1996 10:29

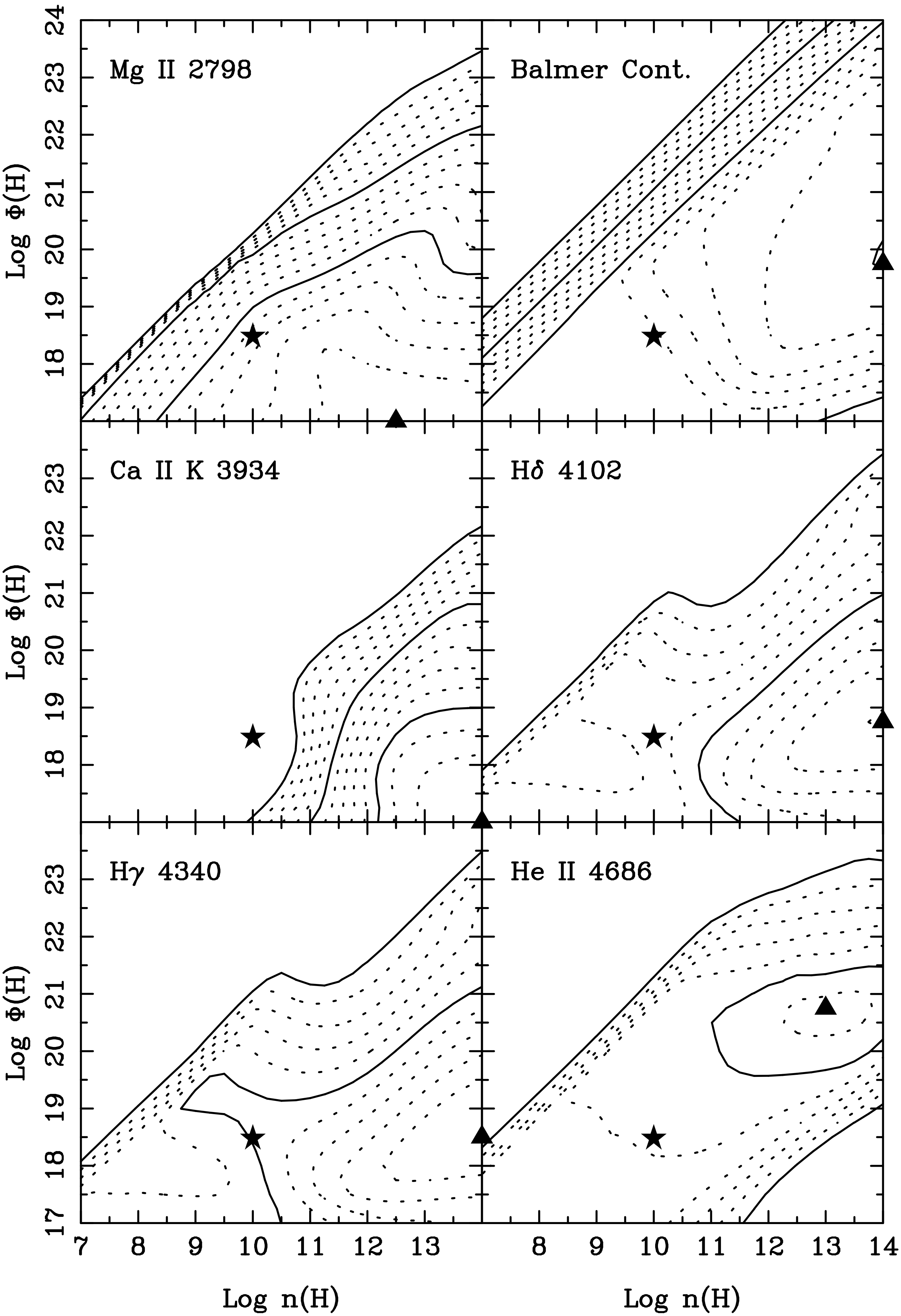

korista 19−Nov−1996 10:32

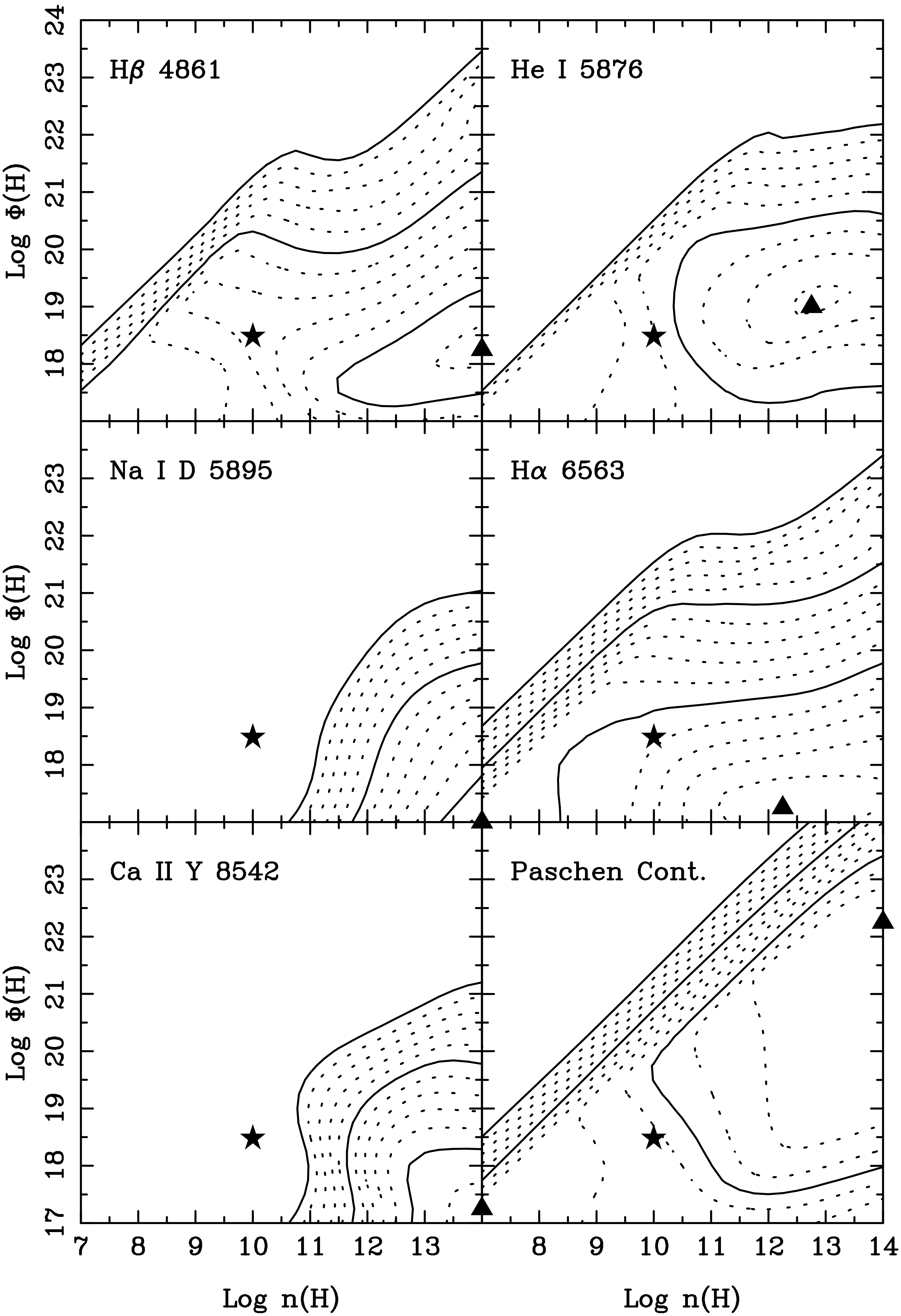

korista 19-Nov-1996 10:35

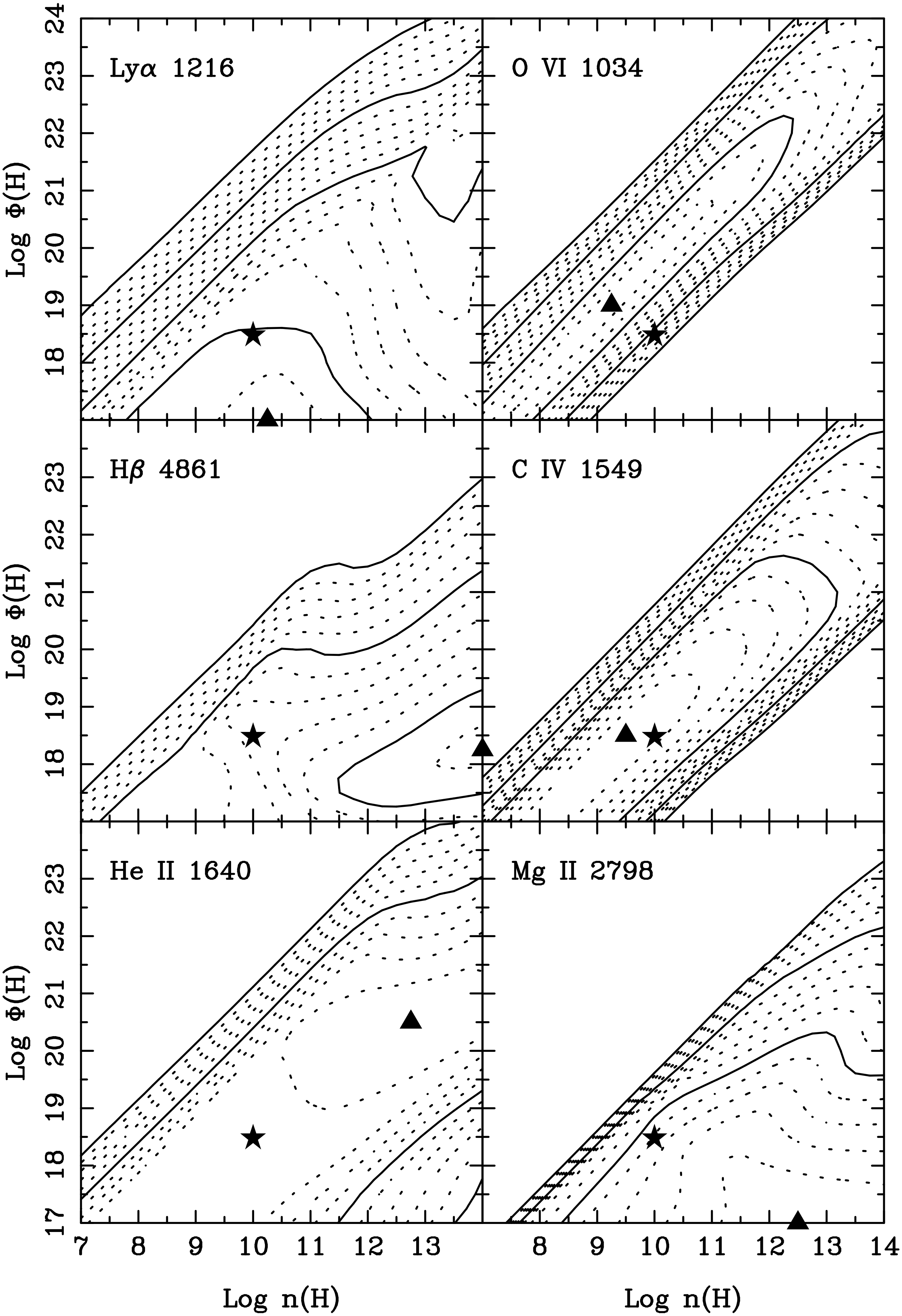

korista 24–Nov–1996 10:57

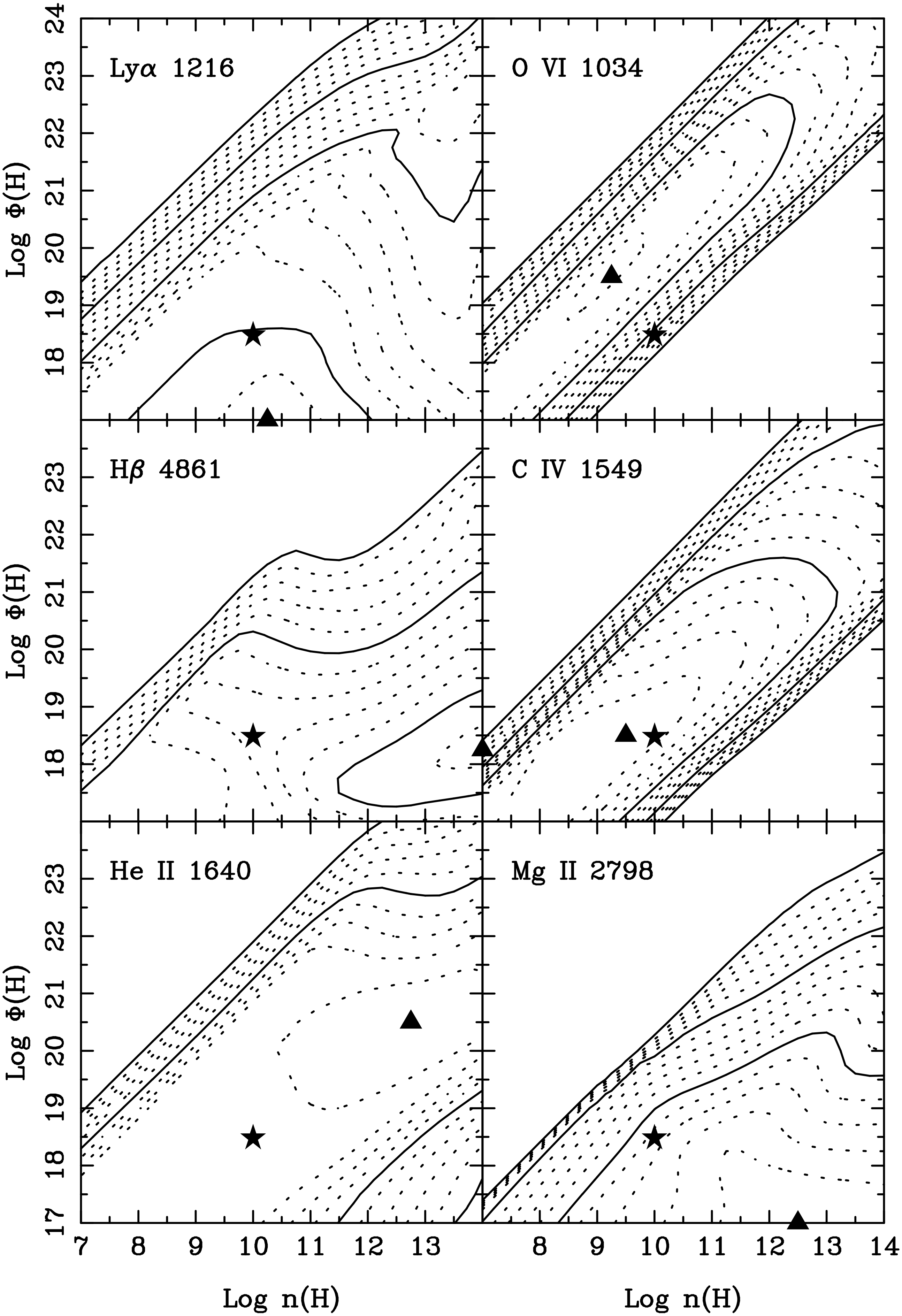
Lyα 1216
O VI 1034
Hβ 4861
C IV 1549
He II 1640
Mg II 2798
Log Φ(H)
Log n(H)
korista 19-Nov-1996 09:28

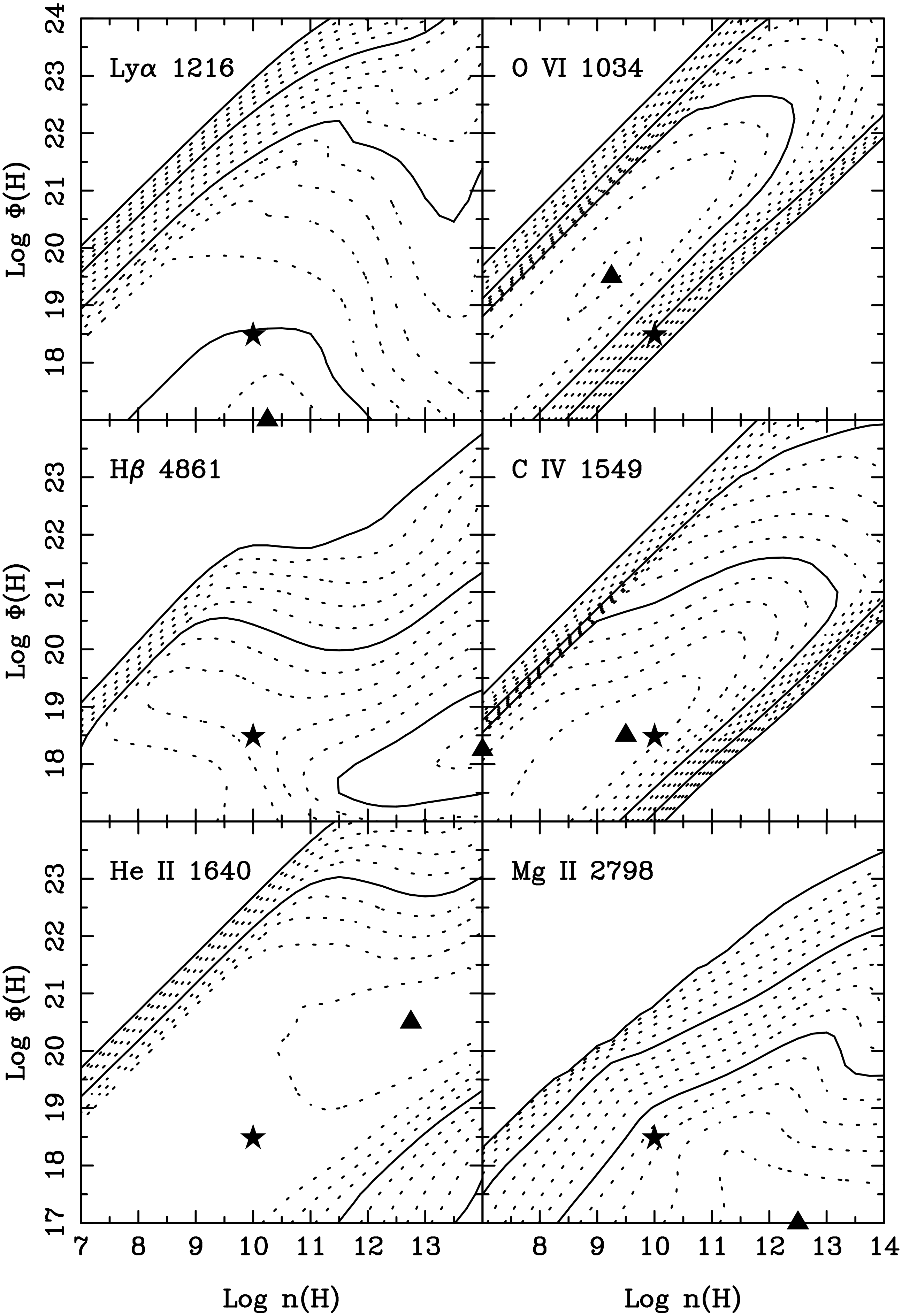

korista 21−Nov−1996 14:57

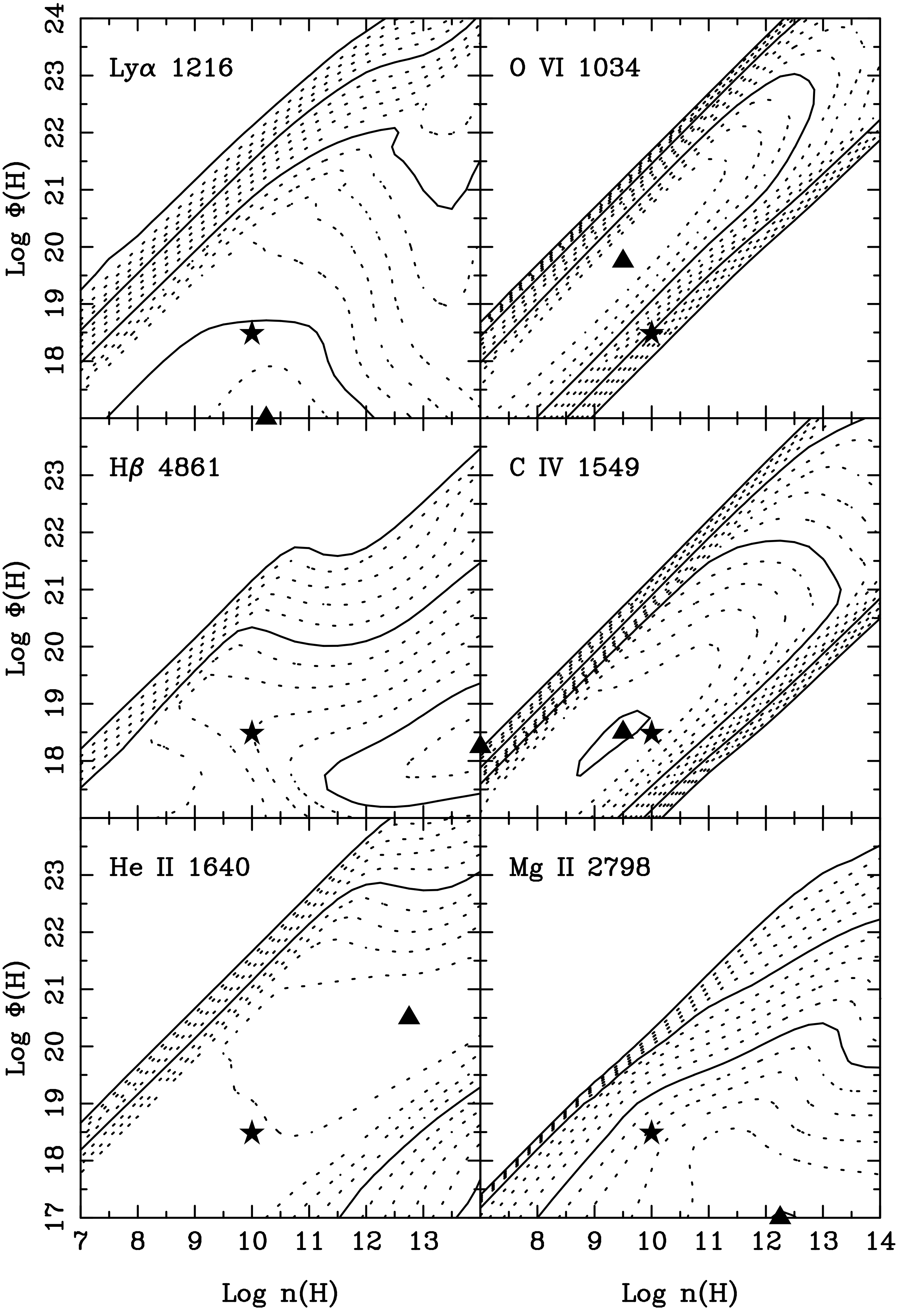

korista 24–Nov–1996 10:04

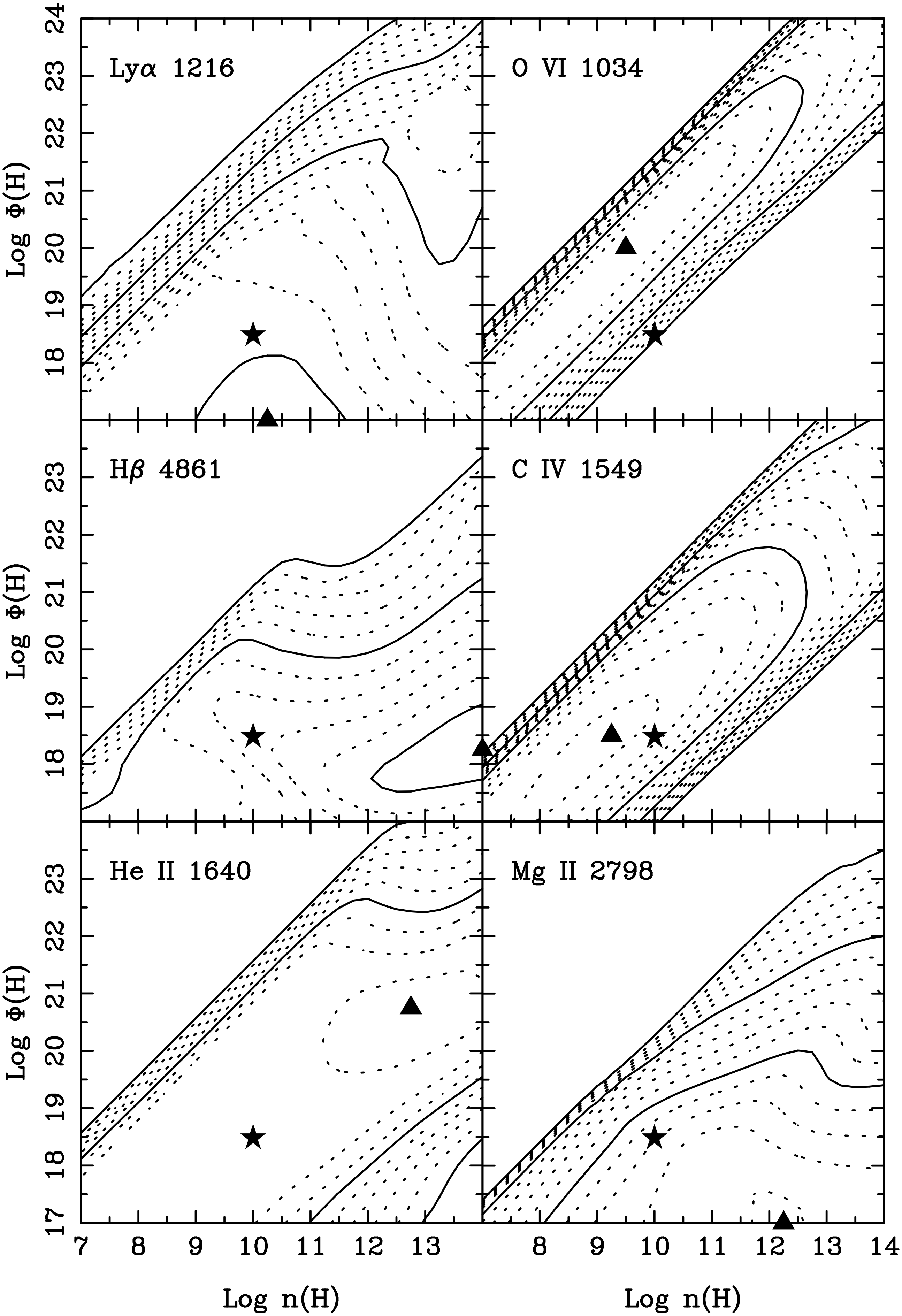

korista 24-Nov-1996 10:30

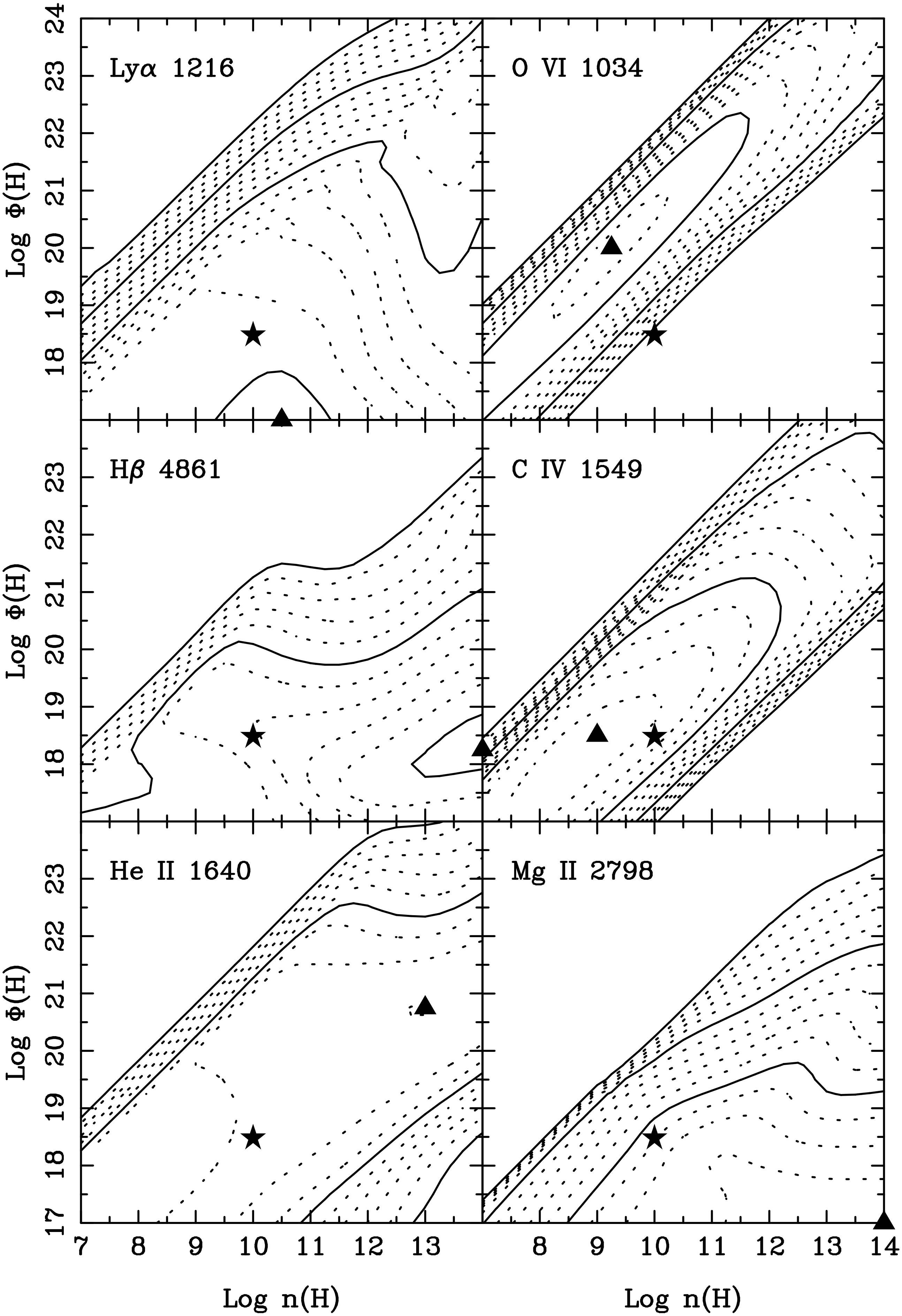

korista 24-Nov-1996 10:38

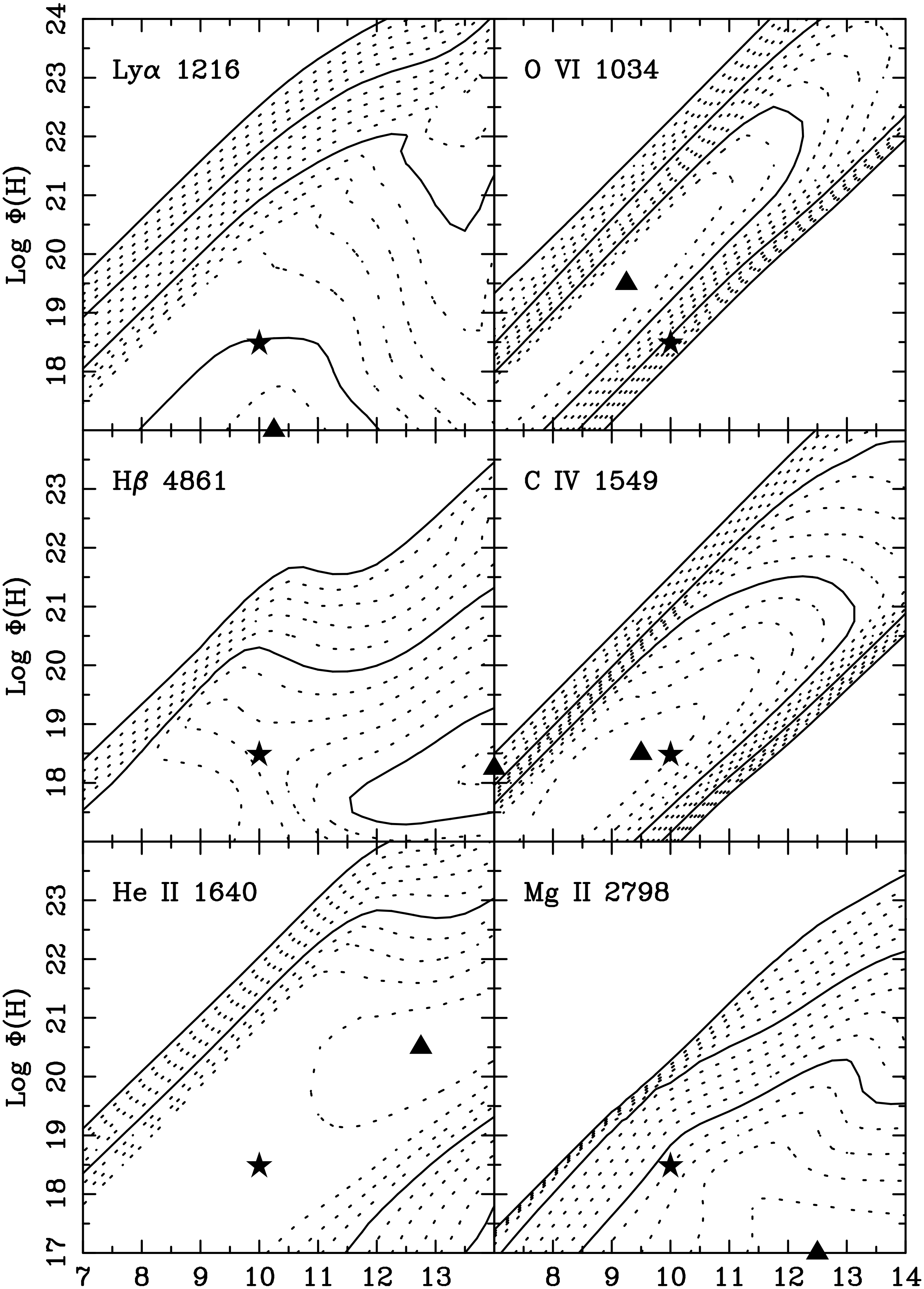

korista 22−Nov−1996 08:31

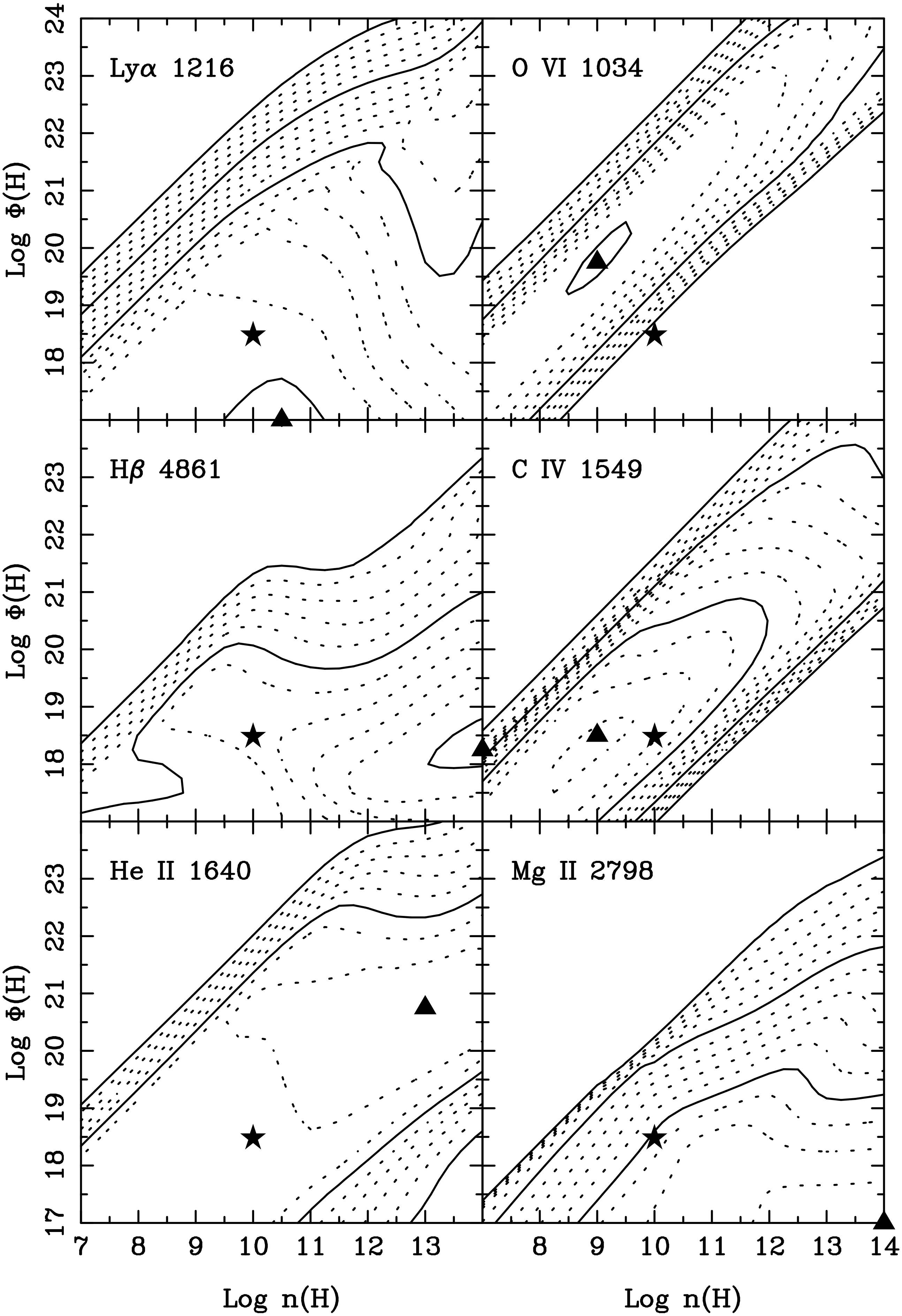

korista 19-Nov-1996 08:52

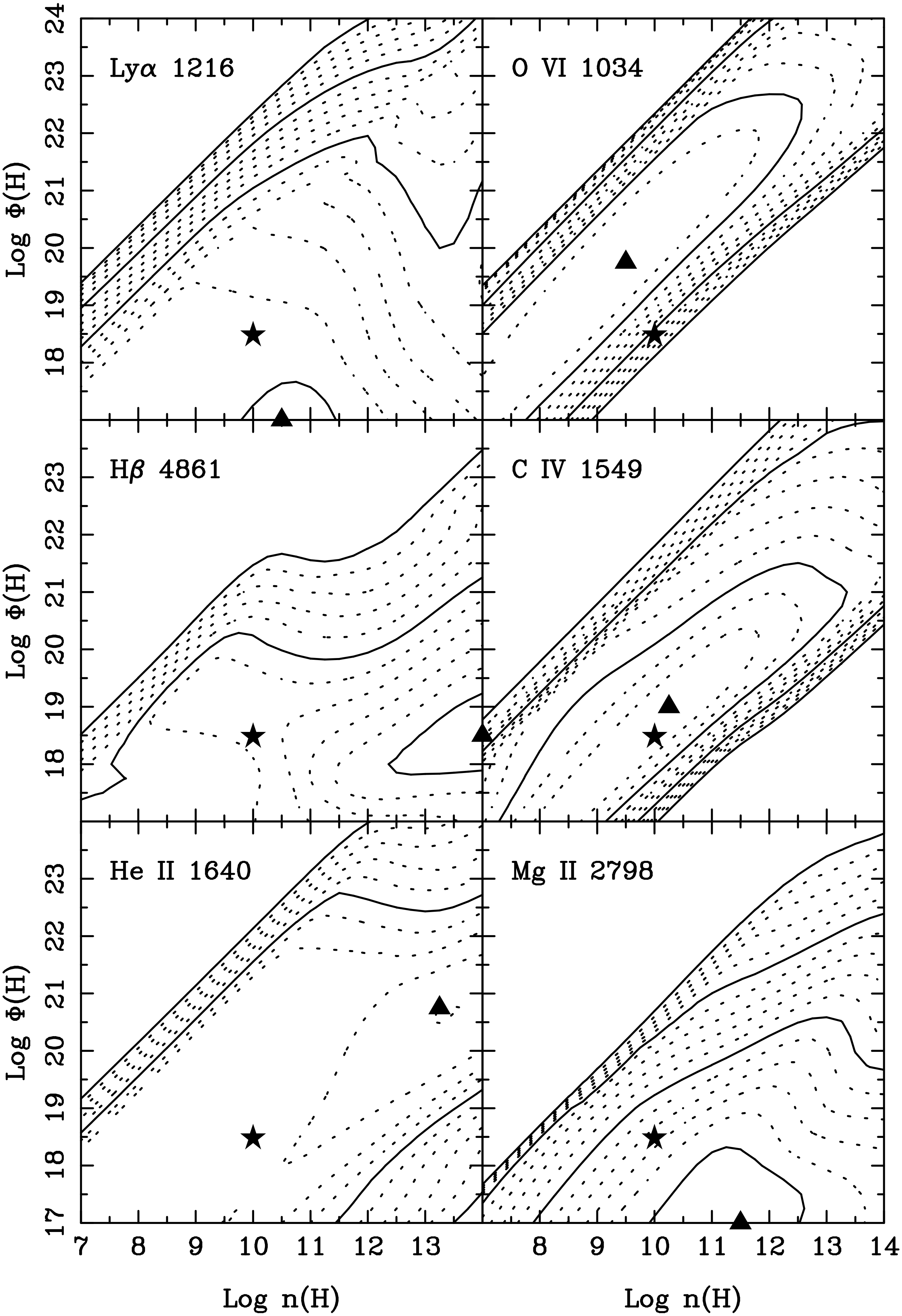

korista 20–Nov–1996 09:04

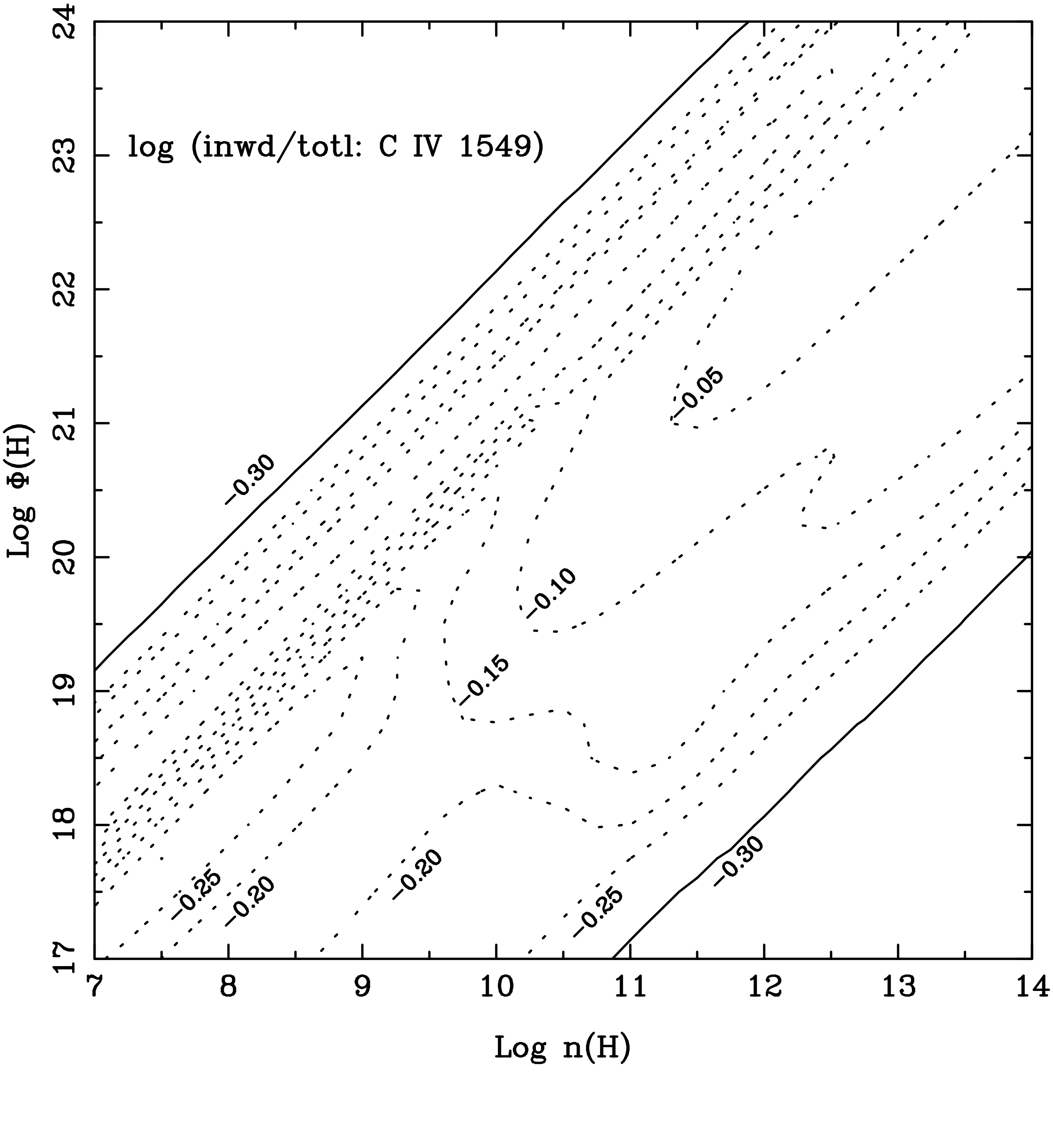

korista 19−Nov−1996 10:00